#### **OPEN ACCESS**



#### COol Companions ON Ultrawide orbiTS (COCONUTS). III. A Very Red L6 Benchmark Brown Dwarf around a Young M5 Dwarf

Zhoujian Zhang (张周健)<sup>1,2,3</sup>, Michael C. Liu<sup>2</sup>, Caroline V. Morley<sup>1</sup>, Eugene A. Magnier<sup>2</sup>, Michael A. Tucker<sup>2</sup>, Zachary P. Vanderbosch<sup>4</sup>, Aaron Do<sup>2</sup>, and Benjamin J. Shappee<sup>2</sup>

The University of Texas at Austin, Department of Astronomy, 2515 Speedway, C1400, Austin, TX 78712, USA; zhoujian@austin.utexas.edu

Institute for Astronomy, University of Hawaii at Manoa, Honolulu, HI 96822, USA

#### Abstract

We present the third discovery from the COol Companions ON Ultrawide orbiTS (COCONUTS) program, the COCONUTS-3 system, composed of the young M5 primary star UCAC4 374-046899 and the very red L6 dwarf WISEA J081322.19-152203.2. These two objects have a projected separation of 61" (1891 au) and are physically associated given their common proper motions and estimated distances. The primary star, COCONUTS-3A, has a mass of  $0.123 \pm 0.006 \, M_{\odot}$ , and we estimate its age as 100 Myr to 1 Gyr based on its stellar activity (via H $\alpha$  and X-ray emission), kinematics, and spectrophotometric properties. We derive its bulk metallicity as  $0.21 \pm 0.07$  dex using empirical calibrations established by older and higher-gravity M dwarfs and find that this [Fe/H] could be slightly underestimated according to PHOENIX models given COCONUTS-3A's younger age. The companion, COCONUTS-3B, has a near-infrared spectral type of L6  $\pm$  1 INT-G, and we infer physical properties of  $T_{\rm eff} = 1362^{+48}_{-73}$  K,  $\log(g) = 4.96^{+0.15}_{-0.34}$  dex,  $R = 1.03^{+0.12}_{-0.06}$   $R_{\rm Jup}$ , and  $M = 39^{+11}_{-18}$   $M_{\rm Jup}$  using its bolometric luminosity, its host star's age, and hot-start evolution models. We construct cloudy atmospheric model spectra at the evolutionbased physical parameters and compare them to COCONUTS-3B's spectrophotometry. We find that this companion possesses ample condensate clouds in its photosphere ( $f_{\text{sed}} = 1$ ) with the data-model discrepancies likely due to the models using an older version of the opacity database. Compared to field-age L6 dwarfs, COCONUTS-3B has fainter absolute magnitudes and a 120 K cooler  $T_{\rm eff}$ . Also, the J-K color of this companion is among the reddest for ultracool benchmarks with ages older than a few hundred megayears. COCONUTS-3 likely formed in the same fashion as stellar binaries given the companion-to-host mass ratio of 0.3 and represents a valuable benchmark to quantify the systematics of substellar model atmospheres.

*Unified Astronomy Thesaurus concepts:* Brown dwarfs (1389); L dwarfs (894); Substellar companion stars (1648); M stars (985)

#### 1. Introduction

Wide-field sky surveys have been a powerful means to construct a large census of planetary-mass and substellar objects in the solar neighborhood, allowing us to investigate star formation at the very low mass end. These surveys also have helped to establish a photometric sequence of ultracool dwarfs spanning M, L, T, and Y dwarfs (e.g., Vrba et al. 2004; Best et al. 2021; Kirkpatrick et al. 2021), as well as to find peculiar objects, including L dwarfs with much redder infrared colors and fainter absolute magnitudes than field objects with similar spectral types (e.g., Gizis et al. 2012; Liu et al. 2013; Schneider et al. 2014; Kellogg et al. 2015; Faherty et al. 2016; Liu et al. 2016; Schneider et al. 2017).

The anomalous photometry of these unusually red L dwarfs suggests that they have more dusty atmospheres (e.g., Saumon & Marley 2008) or a stronger thermochemical instability in their atmospheres (e.g., Tremblin et al. 2016) than normal field dwarfs. Many unusually red L dwarfs have low surface gravities, and their anomalous spectrophotometry thus suggests a gravity dependence of ultracool dwarfs' atmospheric

Original content from this work may be used under the terms of the Creative Commons Attribution 4.0 licence. Any further distribution of this work must maintain attribution to the author(s) and the title of the work, journal citation and DOI.

properties during the L/T tradition (e.g., Metchev & Hillenbrand 2006; Liu et al. 2016; Faherty et al. 2016; Tremblin et al. 2017). However, a number of red L dwarfs likely have old ages (≥1 Gyr), as they are not associated with any young stars or moving groups and have no low-gravity spectral features (e.g., Looper et al. 2008; Kirkpatrick et al. 2010; Allers & Liu 2013).

Spectroscopic characterization of unusually red L dwarfs relies on cloudy and disequilibrium model atmospheres. However, these models are challenged by the uncertainties in opacity line lists, the assumption of radiative-convective equilibrium, and the presence of complex, patchy, timeevolving clouds (e.g., Marley & Robinson 2015; Showman et al. 2020; Zhang 2020). Also, modeling efforts are still needed to reconcile the discrepancies between model predictions and the observed photometric sequence of ultracool dwarfs, particularly near the L/T transition (e.g., Figures 22–24 of Liu et al. 2016). To improve the performance of these models, ultracool dwarfs that are either wide-orbit companions to stars or members of nearby associations are essential benchmarks. The ages and metallicities of these objects can be independently inferred from their associated stars and can therefore identify specific shortcomings of model assumptions and directly quantify the systematic errors of model predictions (e.g., Zhang et al. 2020, 2021c).

<sup>&</sup>lt;sup>3</sup> Visiting Astronomer at the Infrared Telescope Facility, which is operated by the University of Hawaii under contract 80HQTR19D0030 with the National Aeronautics and Space Administration, USA

<sup>&</sup>lt;sup>4</sup> The Division of Physics, Mathematics, and Astronomy, California Institute of Technology, Pasadena, CA 91125, USA Received 2021 November 2; revised 2022 June 25; accepted 2022 June 27; published 2022 August 9

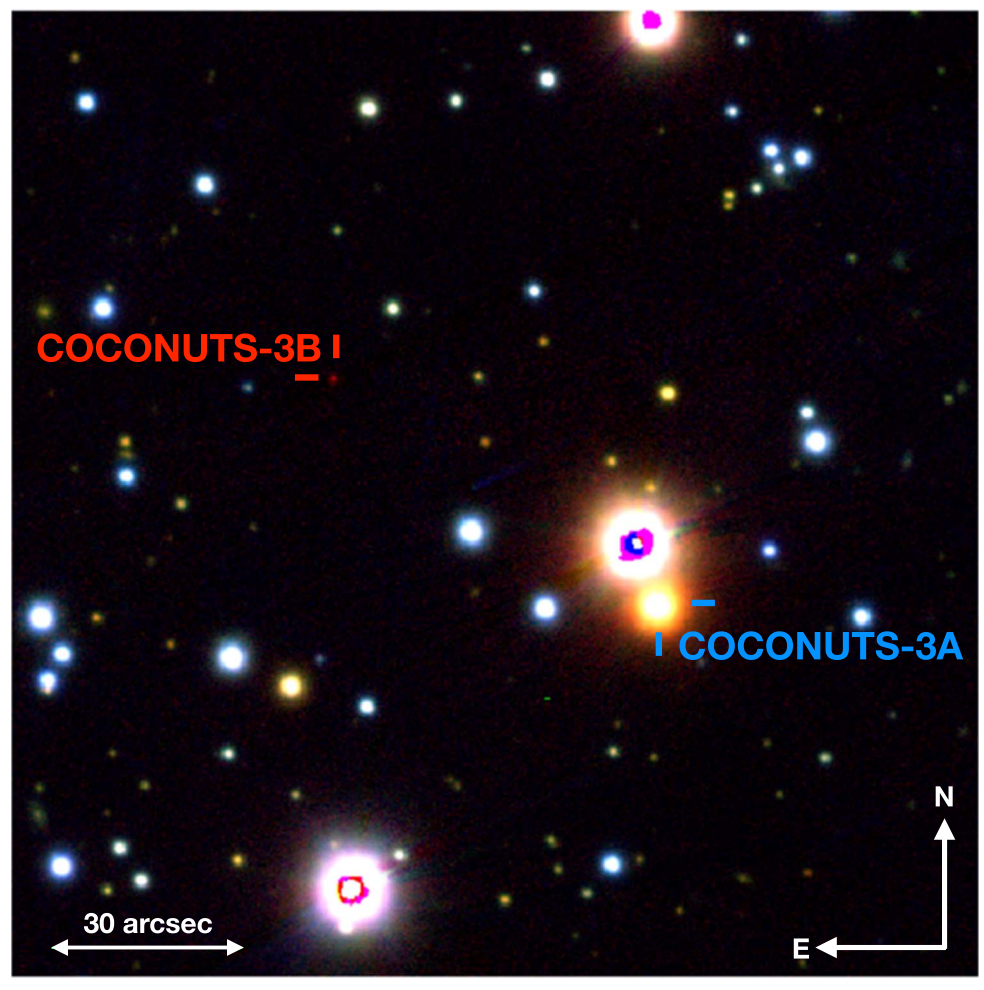


**Figure 1.** The M dwarf primary (COCONUTS-3A) and L dwarf companion (COCONUTS-3B) in the tricolor PS1 image  $(g_{P1})$ : blue,  $i_{P1}$ : green,  $y_{P1}$ : red). The A and B components are separated by  $61\rlap.^{\prime\prime}22\pm0\rlap.^{\prime\prime}03$ , corresponding to a projected physical separation of  $1898\pm2$  au at the primary star's distance. The bright star next to COCONUTS-3A is a background giant star (see Appendix B).

To establish a large census of wide-orbit (\$\ge 500\) au) benchmark companions, we are conducting the COol Companions ON Ultrawide orbiTS (COCONUTS) program by targeting 300,000 stars within 100 pc selected from Gaia. Mining astrometry and photometry from wide-field sky surveys (e.g., Pan-STARRS1 (PS1), Chambers et al. 2016; AllWISE, Wright et al. 2010; Cutri 2014; and CatWISE2020 (CatWISE), Marocco et al. 2021]), we have searched for candidate companions that have consistent proper motions as their host stars (with projected separations  $<10^4$  au) and the optical and infrared colors and magnitudes expected for planetary-mass objects and brown dwarfs (e.g., Best et al. 2018). We then conducted ground-based follow-up observations to confirm the companionship and substellar nature of the new wide-orbit companions. Our first discovery, COCONUTS-1AB (Zhang et al. 2020), is composed of a very old  $(7.3^{+2.8}_{-1.6} \text{ Gyr})$  white dwarf primary and a T4 brown dwarf companion ( $69^{+2}_{-3} M_{\text{Jup}}$ ), which we use to test the high-gravity regime of cloudless model atmospheres (Marley et al. 2021). Our second discovery, COCONUTS-2Ab (Zhang et al. 2021b), is composed of a young (100-800 Myr) M3 primary star with a T9 super-Jupiter companion (6  $\pm$  2  $M_{Jup}$ ), which is the nearest imaged planetarymass object to our solar system and also the second imaged exoplanet whose physical properties overlap both hot- and cold-start formation models.

Here we report the third COCONUTS discovery, a system with a young M dwarf primary star (UCAC4 374–046899; hereafter COCONUTS-3A) with a very red L dwarf companion (WISEA J081322.19–152203.2; hereafter COCONUTS-3B), which was previously identified as a free-floating object by Schneider et al. (2017). We describe the system in Section 2 and our spectroscopic follow-up observations in Section 3. We then study the physical properties of the primary star and the companion in Sections 4 and 5, respectively, followed by a brief summary in Section 6.

#### 2. The COCONUTS-3 System

Figure 1 shows the COCONUTS-3 system and its neighborhood. Based on Gaia EDR3 (Gaia Collaboration et al. 2016, 2021), COCONUTS-3A has a parallax of  $32.33\pm0.02$  mas (distance  $=30.88\pm0.02$  pc; Bailer-Jones et al. 2021) and a proper motion of  $(\mu_{\alpha}\cos\delta,\,\mu_{\delta})=(-131.02\pm0.02,\,+93.39\pm0.02)$  mas yr $^{-1}$ , consistent with the value of  $(-120.9\pm4.4,\,+92.1\pm5.3)$  mas yr $^{-1}$  from CatWISE (Marocco et al. 2021) $^{5}$  and  $(-126.4\pm4.4,\,+84.3\pm3.3)$  mas yr $^{-1}$  from PS1 (Chambers

<sup>&</sup>lt;sup>5</sup> The offset correction in coordinates and proper motions suggested by Marocco et al. (2021) has been incorporated in all CatWISE proper motions used in this work.

et al. 2016; Magnier et al. 2020). The Gaia astrometry of this star is reliable and consistent with the five-parameter single-star model, since it is determined from 20 visibility periods with a mild renormalized unit weight error of 1.14 (Lindegren 2018), suggesting that COCONUTS-3A is single. Based on BANYAN  $\Sigma$  (Gagné et al. 2018) and Gaia astrometry, this star is not associated with any known young moving groups. Also, COCONUTS-3A is a mid-M dwarf, given its optical and near-infrared spectroscopy (Section 4.2).

COCONUTS-3B is a previously known, very red L dwarf identified by Schneider et al. (2017) using Two Micron All Sky Survey (2MASS) and AllWISE photometry. Schneider et al. (2017) assigned an L7 spectral type using  $R \approx 3500$  CTIO/ ARCoIRIS near-infrared (0.8–2.4 µm) spectra with a signal-tonoise ratio (S/N) of only 8 pixel<sup>-1</sup> near the J-band peak. Based on proper motions computed from 2MASS and AllWISE astrometry, they suggested that this L dwarf is a possible member of the Argus (with an 87% membership probability from BANYAN II; Malo et al. 2013; Gagné et al. 2014) or Carina-Near (with a 97% membership probability from the Rodriguez et al. 2013 convergent point tool) moving group. However, Schneider et al. (2017) cautioned that the distances predicted by BANYAN II (15  $\pm$  2 pc) and the Rodriguez et al. (2013) convergent point tool (17 pc), assuming young moving group membership, are both significantly closer than the object's photometric distance of  $31 \pm 6$  pc (derived using  $K_{S,2\text{MASS}}$ , spectral type, and empirical relations between absolute magnitudes and spectral types by Dupuy & Liu 2012). We update this object's photometric distance to be  $32 \pm 7$  pc based on our analysis in Section 5.2, which is independent from the physical association between this object and COCONUTS-3A (see below). Using BANYAN  $\Sigma$  (Gagné et al. 2018) and this L dwarf's photometric distance, we find CatWISE proper its  $(\mu_{\alpha}\cos\delta, \mu_{\delta}) = (-120.8 \pm 6.9, +92.5 \pm 7.6) \text{ mas yr}^{-1}, \text{ cor-}$ responds to a 30% Carina-Near and 28% Argus membership. In addition, this object's PS1 proper motion,  $(-112.6 \pm 21.0)$  $+101.1 \pm 21.0$ ) mas yr<sup>-1</sup>, corresponds to a 19% Carina-Near and 57% Argus membership. Thus, young moving group membership for COCONUTS-3B seems unlikely, but this object's photometric distance and proper motions agree very well with those of COCONUTS-3A.

We conclude that COCONUTS-3B is a comoving companion to the field dwarf COCONUTS-3A (Figure 2). Based on their CatWISE coordinates, the A and B components are separated by  $61\rlap.{''}46\pm0\rlap.{''}04$ , meaning a projected physical separation of  $1891\pm2$  au at the primary star's distance. The properties of COCONUTS-3AB are summarized in Table 1.

#### 3. Observations

#### 3.1. Spectroscopy of the M Dwarf Primary: COCONUTS-3A

#### 3.1.1. UH 2.2 m/SNIFS

We obtained optical (3500–9100 Å) spectra of COCO-NUTS-3A on UT 2019 October 7 using the SuperNova Integral Field Spectrograph (SNIFS; Aldering et al. 2002; Lantz et al. 2004) mounted on the University of Hawai'i's 2.2 m telescope. SNIFS is a  $6'' \times 6''$  integral field spectrograph and provides a spectral resolution of  $R \approx 1200$ . We took one 1800 s exposure for our target and then followed the pipeline described in Bacon et al. (2001) to extract the 1D spectrum, comprising dark, bias, and flat-field corrections, wavelength calibration,

and sky subtraction. The dispersion in wavelength calibration is 0.55 Å for the blue channel (3500–4700 Å) and 0.08 Å for the red channel (5300–9100 Å). We flux-calibrated the 1D spectrum using spectrophotometric standard stars observed during the same night, LTT 2415, Feige 110, HR 3454, and GD 71. Although the night was nonphotometric, only the relative fluxes of the SNIFS spectra (and GMOS spectra in Section 3.1.2) are used in our subsequent analysis and are thus reliable. Our resulting SNIFS spectrum has air wavelengths, with S/N = 28 at 6700 Å and 74 at 8200 Å, and also exhibits  ${\rm H}\alpha$  emission.

#### 3.1.2. Gemini/GMOS

The optical (6400–8900 Å) spectra of COCONUTS-3A were also acquired with the GMOS spectrograph (Hook et al. 2004) at the Gemini-North Telescope (queue program GN-2019B-Q-139; PI: Z. Zhang) on UT 2019 December 12 in order to search for lithium  $\lambda\lambda 6708$  absorption. The R831 grating was used in conjunction with the GG-455 filter and the 0."5 long slit  $(R \approx 4400)$ . One 330 s exposure was taken with central wavelengths of 7600, 7650, and 7700 Å (i.e., three exposures in total). Such wavelength dithering compensates for the detectors' interchip gaps (≈38 Å in our data), enabling continuous wavelength coverage. Using the Gemini IRAF data reduction package, we performed dark, bias, and flat-fielding corrections, cosmic-ray rejection, wavelength calibration, and sky subtraction. The dispersion in the wavelength calibration is 0.01 Å. We then flux-calibrated our extracted spectra by using a spectrophotometric standard, Feige 34, observed on UT 2019 November 28. This calibration produces reliable relative fluxes for the GMOS spectra for our subsequent analysis, which does not require absolute fluxes. We computed the weighted average of all three spectra with flux uncertainties propagated to provide the final GMOS spectrum of COCONUTS-3A, with air wavelengths and S/N = 125 at 6700 Å and 380 at 8200 Å.

#### 3.1.3. IRTF/SpeX

Near-infrared (0.7–2.5  $\mu$ m) spectra of COCONUTS-3A were observed using the NASA Infrared Telescope Facility (IRTF) on UT 2019 April 26. We used the SpeX spectrograph (Rayner et al. 2003) in the short-wavelength cross-dispersed (SXD) mode with the 0.73 slit ( $R \approx 2000$ ) and took six 120 s exposures in a standard ABBA nodding pattern. We contemporaneously observed an A0V standard star, HD 67725, within a 0.01 airmass of COCONUTS-3A for telluric correction. We reduced the data using version 4.1 of the Spextool software package (Cushing et al. 2004) and obtained a 0.122 Å dispersion in the wavelength calibration. Our resulting SpeX SXD spectrum has vacuum wavelengths with median S/Ns of 135 and 146 pixel<sup>-1</sup> in the J and K bands, respectively.

#### 3.2. Spectroscopy of the L Dwarf Companion: COCONUTS-3B

#### 3.2.1. IRTF/SpeX

We acquired near-infrared (0.7–2.5  $\mu$ m) spectra of COCO-NUTS-3B using IRTF/SpeX in prism mode with the 0."8 slit ( $R \approx 75$ ) on UT 2019 April 7 and UT 2019 November 2. We took a total of 74 exposures of 120 s each in an ABBA pattern and contemporaneously observed multiple A0V standard stars (HD 78955, HD 82724, HD 89911, HD 72366, and HD 71580)

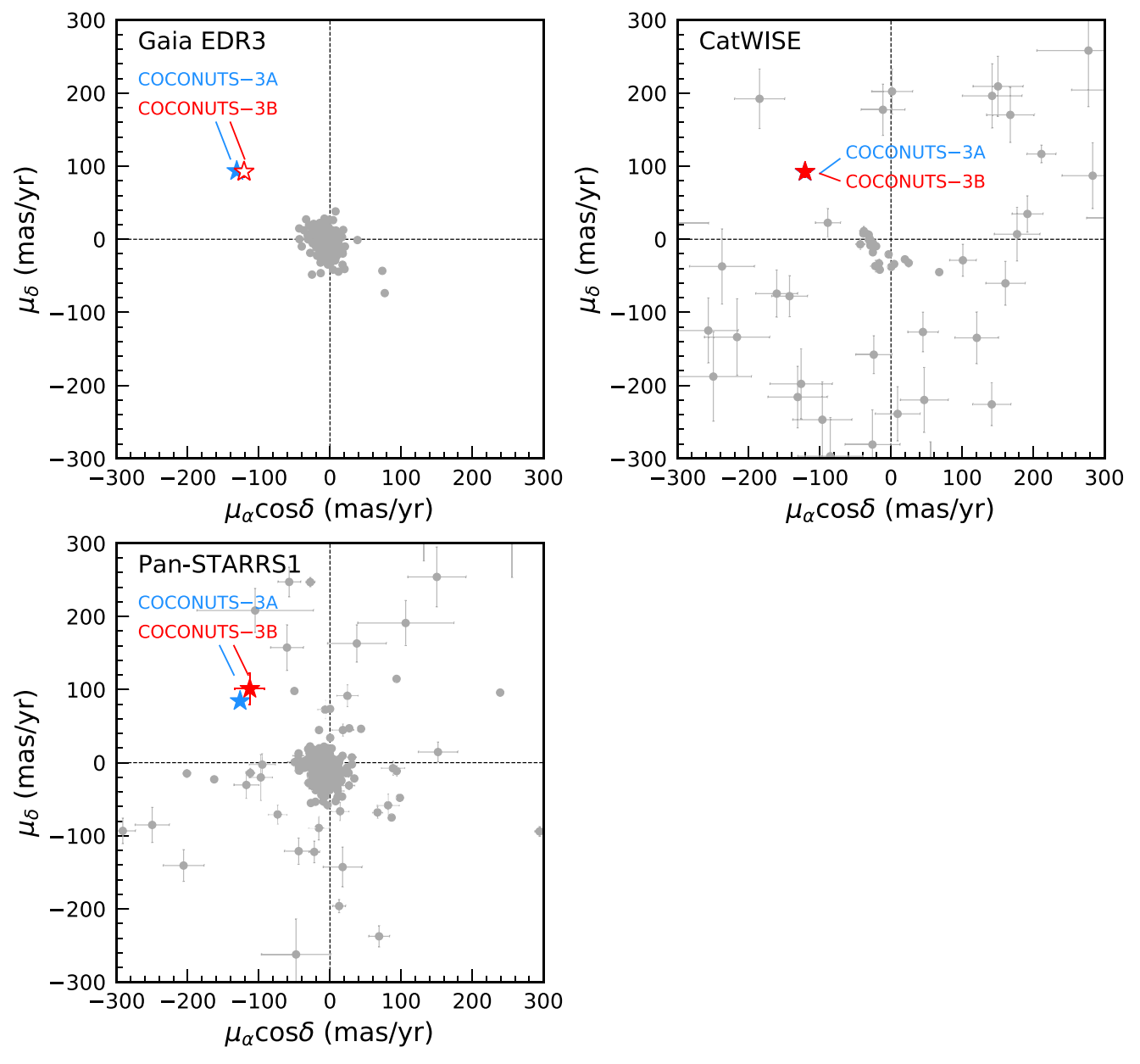


Figure 2. Proper motions of COCONUTS-3A (blue) and 3B (red) from Gaia EDR3 (top left), CatWISE (top right), and PS1 (bottom left). Since the companion has no Gaia detection, we plot its CatWISE proper motion (red open symbol) in the top left panel. The two objects have very consistent CatWISE proper motions, so their symbols overlap in the top right panel. Proper motions (if S/N > 5) of nearby stars (gray) within 15' are overlaid in each panel. The common proper motions between the A and B components are demonstrated by these diagrams and validate their physical association.

to perform the telluric correction, given that the airmass of the companion spanned a wide range over long exposures. We divided the raw spectroscopic data of COCONUTS-3B into five subsets, with each set calibrated by a telluric standard with a <0.1 airmass difference. The dispersion in wavelength calibration of the prism data is 5.9 Å. Combining all five telluric-corrected spectra using a robust weighted mean, we obtained the SpeX prism spectrum with vacuum wavelengths and a median  $S/N = 53 \text{ pixel}^{-1}$  in the J band.

#### 3.2.2. Gemini/GNIRS

The near-infrared (0.9–2.5  $\mu$ m) spectra of COCONUTS-3B were observed with the Gemini-North GNIRS spectrograph (Elias et al. 2006) on UT 2019 November 12 (queue program GN-2019B-Q-139; PI: Z. Zhang) with a higher

spectral resolution ( $R \approx 750$ ) than the SpeX prism data. The cross-dispersed (XD) mode was used with the 32 I/mm grating, short camera (0."15 pixel<sup>-1</sup>), 0."675 slit. Eight exposures were taken with 222 s each in an ABBA pattern. Also, an A0V telluric standard star, HIP 37787, was contemporaneously observed within a 0.05 airmass of COCONUTS-3B. We reduced the data using a modified version of Spextool (K. Allers 2022, private communication; see also Vacca et al. 2003; Cushing et al. 2004; Section 4.4 of Kirkpatrick et al. 2011) and obtained a dispersion of 0.8 Å in wavelength calibration. Our resulting GNIRS XD spectrum has vacuum wavelengths and a median S/N = 45 pixel<sup>-1</sup> in the J band.

Table 1
Properties of COCONUTS-3

Properties  Spectral type Age (Myr) [Fe/H] (dex)  R.A., decl. (epoch J2000; hms, dms) Gaia EDR3 $\mu_{\alpha} \cos \delta$ , $\mu_{\delta}$ (mas yr <sup>-1</sup> ) CatWISE $\mu_{\alpha} \cos \delta$ , $\mu_{\delta}$ (mas yr <sup>-1</sup> ) PS1 $\mu_{\alpha} \cos \delta$ , $\mu_{\delta}$ (mas yr <sup>-1</sup> ) Gaia EDR3 parallax (mas) Distance (pc) Tangential velocity (km s <sup>-1</sup> )	Value  M5.5±0.5 (opt.), M4.5±0.5 (NIR)  100–1000  0.21 ± 0.07  Astrometry a	References This work This work This work This work	Value L6±1 INT-G	References This work	
Age (Myr) [Fe/H] (dex) $\begin{array}{c} \text{R.A., decl. (epoch J2000; hms, dms)} \\ \text{Gaia EDR3} \ \mu_{\alpha} \cos \delta, \ \mu_{\delta} \ (\text{mas yr}^{-1}) \\ \text{CatWISE} \ \mu_{\alpha} \cos \delta, \ \mu_{\delta} \ (\text{mas yr}^{-1}) \\ \text{PS1} \ \mu_{\alpha} \cos \delta, \ \mu_{\delta} \ (\text{mas yr}^{-1}) \\ \text{Gaia EDR3 parallax (mas)} \\ \text{Distance (pc)} \end{array}$	$100-1000 \\ 0.21 \pm 0.07$ Astrometry a	This work This work			
[Fe/H] (dex)  R.A., decl. (epoch J2000; hms, dms) Gaia EDR3 $\mu_{\alpha} \cos \delta$ , $\mu_{\delta}$ (mas yr <sup>-1</sup> ) CatWISE $\mu_{\alpha} \cos \delta$ , $\mu_{\delta}$ (mas yr <sup>-1</sup> ) PS1 $\mu_{\alpha} \cos \delta$ , $\mu_{\delta}$ (mas yr <sup>-1</sup> ) Gaia EDR3 parallax (mas) Distance (pc)	$0.21 \pm 0.07$ Astrometry a	This work			
R.A., decl. (epoch J2000; hms, dms) Gaia EDR3 $\mu_{\alpha} \cos \delta$ , $\mu_{\delta}$ (mas yr <sup>-1</sup> ) CatWISE $\mu_{\alpha} \cos \delta$ , $\mu_{\delta}$ (mas yr <sup>-1</sup> ) PS1 $\mu_{\alpha} \cos \delta$ , $\mu_{\delta}$ (mas yr <sup>-1</sup> ) Gaia EDR3 parallax (mas) Distance (pc)	Astrometry a				
Gaia EDR3 $\mu_{\alpha} \cos \delta$ , $\mu_{\delta}$ (mas yr <sup>-1</sup> ) CatWISE $\mu_{\alpha} \cos \delta$ , $\mu_{\delta}$ (mas yr <sup>-1</sup> ) PS1 $\mu_{\alpha} \cos \delta$ , $\mu_{\delta}$ (mas yr <sup>-1</sup> ) Gaia EDR3 parallax (mas) Distance (pc)	<u>_</u>	and Kinematics			
Gaia EDR3 $\mu_{\alpha} \cos \delta$ , $\mu_{\delta}$ (mas yr <sup>-1</sup> ) CatWISE $\mu_{\alpha} \cos \delta$ , $\mu_{\delta}$ (mas yr <sup>-1</sup> ) PS1 $\mu_{\alpha} \cos \delta$ , $\mu_{\delta}$ (mas yr <sup>-1</sup> ) Gaia EDR3 parallax (mas) Distance (pc)		Illionades			
CatWISE $\mu_{\alpha} \cos \delta$ , $\mu_{\delta}$ (mas yr <sup>-1</sup> ) PS1 $\mu_{\alpha} \cos \delta$ , $\mu_{\delta}$ (mas yr <sup>-1</sup> ) Gaia EDR3 parallax (mas) Distance (pc)	08:13:18.84, -15:22:39.6	Gaia16, 20	08:13:22.30, -15:22:04.4	Cham16, Magn2	
PS1 $\mu_{\alpha} \cos \delta$ , $\mu_{\delta}$ (mas yr <sup>-1</sup> ) Gaia EDR3 parallax (mas) Distance (pc)	$-131.02 \pm 0.02,  93.39 \pm 0.02$	Gaia16, 20			
Gaia EDR3 parallax (mas) Distance (pc)	$-120.9 \pm 4.4, 92.1 \pm 5.3$	Maro21	$-120.8 \pm 6.9, 92.5 \pm 7.6$	Maro21	
Distance (pc)	$-126.4 \pm 4.4,  84.3 \pm 3.3$	Cham16, Magn20	$-112.6 \pm 21.0, 101.1 \pm 21.0$	Cham16, Magn2	
Distance (pc)	$32.33 \pm 0.02$	Gaia16, 20			
	$30.88 \pm 0.02$	Bail21	$32\pm7^{\mathrm{a}}$	This work	
	$23.57 \pm 0.02$	This work	$22.3 \pm 1.1$	This work	
Radial velocity (km s <sup>-1</sup> )	$41 \pm 60$	This work			
Position angle (east of north; deg)		•••	$54.75 \pm 0.03$	This work	
Projected separation			$61\rlap.{''}22 \pm 0\rlap.{''}03~(1891 \pm 1.6~au)$	This work	
	Spectrophoton	netric Properties			
Gaia DR2 G (mag)	$14.0348 \pm 0.0005$	Gaia16, 18			
Gaia DR2 BP (mag)	$15.835 \pm 0.004$	Gaia16, 18	•••		
Gaia DR2 RP (mag)	$12.748 \pm 0.002$	Gaia16, 18	•••		
PS1 g (mag)	$16.194 \pm 0.003$	Cham16	•••		
PS1 r (mag)	$14.953 \pm 0.003$	Cham16	•••		
PS1 i (mag)	$13.311 \pm 0.003^{b}$	Cham16	$22.02 \pm 0.25$	Cham16	
PS1 z (mag)	$12.594 \pm 0.035^{b}$	Cham16	$20.60 \pm 0.07$	Cham16 Cham16	
PS1 y (mag)	$12.196 \pm 0.005^{b}$	Cham16	$19.53 \pm 0.05$		
VHS J (mag)	$12.1354 \pm 0.0007$	McMa13	$17.124 \pm 0.013$	McMa13	
VHS $K_S$ (mag)	$11.3509 \pm 0.0009$	McMa13	$15.050 \pm 0.012$	McMa13	
2MASS J (mag)	$12.18 \pm 0.01^{c}$	This work	$17.19 \pm 0.03^{\circ}$	This work	
2MASS H (mag)	$11.59 \pm 0.05^{\circ}$	This work	$15.89 \pm 0.06^{\circ}$	This work	
2MASS $K_S$ (mag)	$11.32 \pm 0.01^{\circ}$	This work	$15.02 \pm 0.03^{\circ}$	This work	
MKO Y (mag)	$12.71 \pm 0.05^{c}$	This work	$18.39 \pm 0.07^{\circ}$	This work	
MKO $J$ (mag)	$12.14 \pm 0.01^{\circ}$	This work	$17.09 \pm 0.03^{\circ}$	This work	
MKO H (mag)	$11.61 \pm 0.05^{c}$	This work	$15.95 \pm 0.06^{\circ}$	This work	
MKO K (mag)	$11.30 \pm 0.01^{c}$	This work	$14.99 \pm 0.03^{\circ}$	This work	
W1 (mag)	$9.825 \pm 0.013$	Maro21	$14.037 \pm 0.014$	Maro21	
W2 (mag)	$9.645 \pm 0.009$	Maro21	$13.534 \pm 0.012$	Maro21	
$EW(H\alpha)$ (Å)	$-2.9 \pm 0.2, -7.18 \pm 0.02$	This work			
	Physical	Properties			
$\log(L_{\mathrm{X}})$ (dex)	$28.3 \pm 0.2$	This work			
$\log(L_{\rm bol}/L_{\odot})$ (dex)	$-2.80\pm0.04$	This work	$-4.45 \pm 0.03$	This work	
$P_{\rm rot}$ (hr)	>2.7	This work			
$T_{\rm eff}$ (K)	$2966 \pm 85$	This work	$1362_{-73}^{+48}$	This work	
$\log(g)$ (dex)	$5.17 \pm 0.03$	This work	$4.96^{+0.15}_{-0.34}$	This work	
$R \text{ (A: } R_{\odot}; \text{B: } R_{\text{Jup}})$	$0.151 \pm 0.004$	This work	$1.03^{+0.12}_{-0.06}$	This work	
$M \text{ (A: } M_{\odot}, B: M_{\text{Jup}})$ $M \text{ (A: } M_{\odot}; B: M_{\text{Jup}})$	$0.123 \pm 0.004$ $0.123 \pm 0.006$	This work	$39^{+11}_{-18}$	This work	

#### Notes

References. Bail21: Bailer-Jones et al. (2021); Cutr03: Cutri et al. (2003); Cham16: Chambers et al. (2016); Gaia16: Gaia Collaboration et al. (2016); Gaia18: Gaia Collaboration et al. (2018b); Gaia20: Gaia Collaboration et al. (2021); McMa13: McMahon et al. (2013); Magn20: Magnier et al. (2020); Maro21: Marocco et al. (2021); Schn17: Schneider et al. (2017).

#### 4. COCONUTS-3A: The M Dwarf Primary Star

#### 4.1. Radial Velocity

We convert the spectra of COCONUTS-3A to the stellar rest frame by comparing with spectral templates. For the optical

spectrum, we use templates from PyHammer (Kesseli et al. 2017), a modified version of the Hammer spectral classification tool (Covey et al. 2007). These templates are constructed using the Baryon Oscillation Spectroscopic Survey of the Sloan Digital Sky Survey (SDSS; Dawson et al. 2013), spanning

<sup>&</sup>lt;sup>a</sup> Photometric distance derived using the object's  $J_{MKO}$  magnitude, the L6 INT-G spectral classification, and the Liu et al. (2016) empirical relations.

<sup>&</sup>lt;sup>b</sup> The  $i_{\rm Pl}/z_{\rm Pl}/y_{\rm Pl}$  photometry of the primary star is saturated.

<sup>&</sup>lt;sup>c</sup> These photometries are synthesized using the objects' near-infrared spectra and VHS broadband photometry (Sections 4.4 and 5.2).

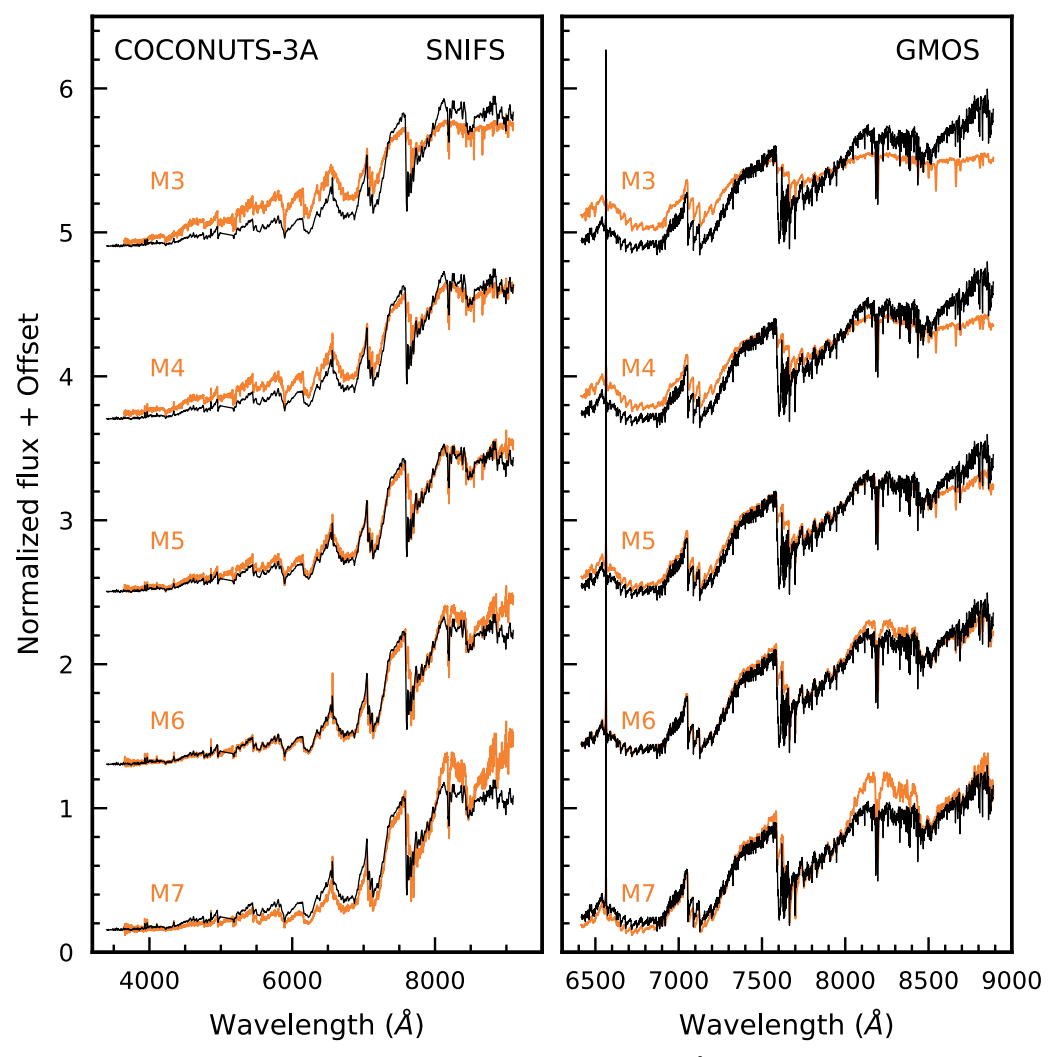


Figure 3. The SNIFS and GMOS spectra of COCONUTS-3A (black) normalized by the flux at 8000 Å. PyHammer M3-M7 spectral templates (Kesseli et al. 2017) are overlaid and scaled by the average flux at 6500-9000 Å. We only show templates with solar metallicity (orange), since the overall morphology of these templates at a given spectral type does not vary significantly with metallicities from -0.5 to +0.5 dex. The spike shown at the short wavelength of our observed GMOS spectrum is the H $\alpha$  emission line discussed in Section 4.5.1. We derive a visual optical spectral type of M5.5  $\pm$  0.5 for COCONUTS-3A.

3650–10200 Å wavelengths in vacuum ( $R \sim 2000$ ), O5–L3 spectral types, and [Fe/H] = -2 to +1 dex (with intervals of 0.5 dex). We first put our SNIFS and GMOS spectra in vacuum following Ciddor (1996). Given that COCONUTS-3A has an optical spectral type of M5.5  $\pm$  0.5 (Section 4.2), we crosscorrelate with all M5 and M6 PyHammer templates (with [Fe/H] = -0.5, 0, and +0.5 dex at each spectral type) over a wavelength range of 6500–8800 Å for both SNIFS and GMOS spectra. We then shift these spectra using the average radial velocity of 120.4 (SNIFS) and 15.0 (GMOS) km s<sup>-1</sup> after confirming that no  $>5\sigma$  outliers exist.

For the near-infrared spectrum, we use Gl213 (M4), Gl268AB (M4.5), and Gl51 (M5) from the IRTF Spectral Library (Cushing et al. 2005; Rayner et al. 2009) as templates, given that COCONUTS-3A has a near-infrared spectral type of M4.5  $\pm$  0.5 (Section 4.2). We cross-correlate the SpeX SXD spectrum of COCONUTS-3A with each template over individual orders 3–7 and then shift the spectrum by using the average value of 58.8 km s $^{-1}$  among all computed radial velocities (no  $>\!5\sigma$  outliers are detected).

Based on the size of 1 resolution pixel, we assign an uncertainty of 250, 68, and 150 km s<sup>-1</sup> to the estimated radial

velocity by SNIFS, GMOS, and SpeX SXD spectra, respectively. We further apply the barycentric correction to each measured radial velocity using Astropy (Astropy Collaboration et al. 2013, 2018) and compute their weighted mean and error, leading to a radial velocity of  $41\pm60\,\mathrm{km\,s^{-1}}$  for COCONUTS-3A.

#### 4.2. Spectral Type

We determine the optical spectral type of COCONUTS-3A using PyHammer (Kesseli et al. 2017), which measures a suite of indices and then compares to those of spectral templates via a weighted least-squares approach. PyHammer contains templates with a range of metallicities, thereby enabling a metallicity estimate along with the spectral type. Kesseli et al. (2017) suggested that the spectral types and metallicities estimated by PyHammer are accurate to  $\pm 1.5$  subtypes and  $\pm 0.4$  dex, respectively. We find that COCONUTS-3A has an index-based spectral type of M6 using both SNIFS and GMOS spectra, with a metallicity of -0.5 and 0 dex, respectively. Visually comparing our observed spectra with the PyHammer spectral templates, we assign a visual type of M5.5  $\pm$  0.5 (Figure 3) and adopt this as the final optical spectral type of the

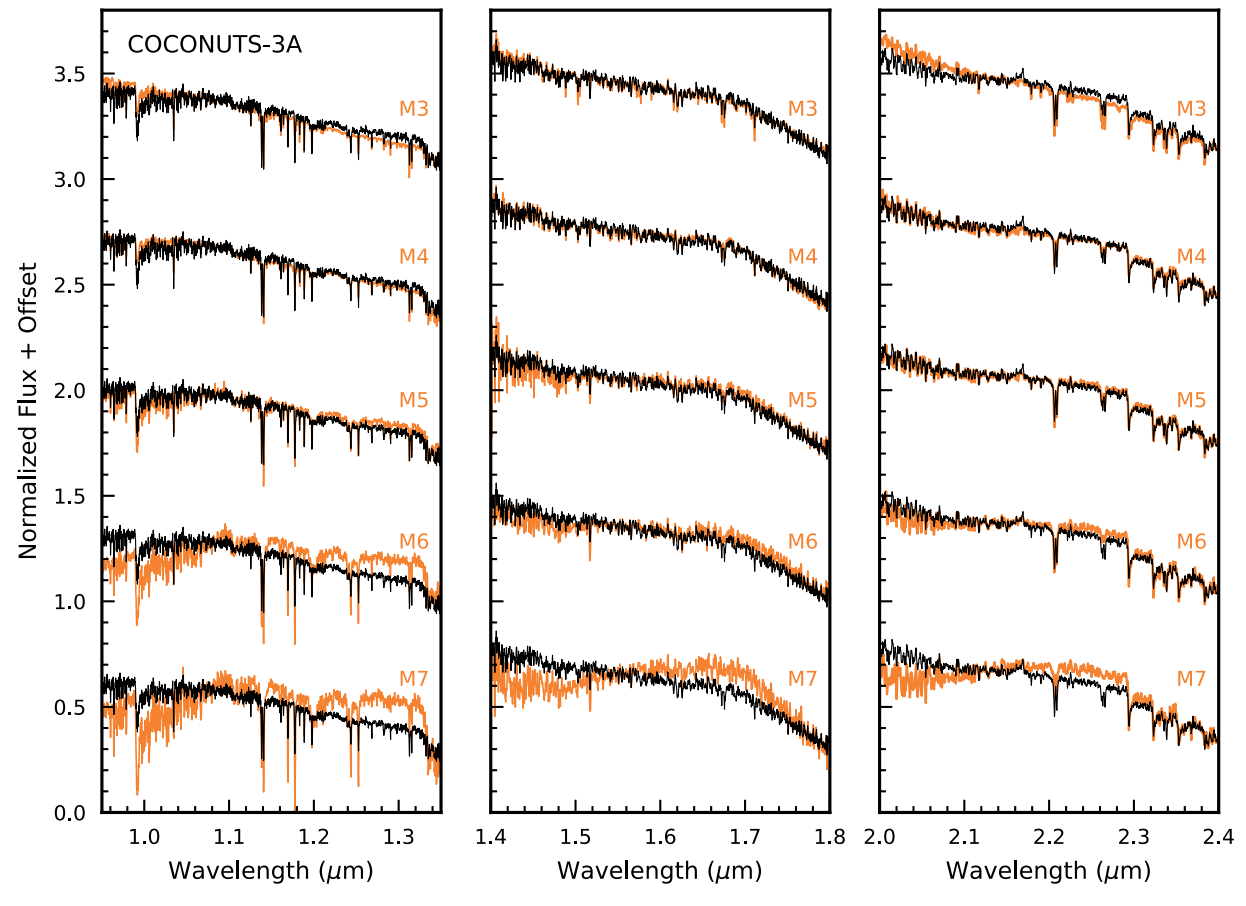


Figure 4. The SpeX SXD spectrum of COCONUTS-3A (black) as compared to the M3-M7 spectral standards (orange) from the IRTF Spectral Library (Cushing et al. 2005; Rayner et al. 2009) in the J (left), H (middle), and K (right) bands: Gl 388 (M3), Gl 213 (M4), Gl 51 (M5), Gl 406 (M6), and Gl 644C (M7). All of these spectra are normalized by their average fluxes in each band. We derive a visual near-infrared spectral type of M4.5  $\pm$  0.5 for COCONUTS-3A.

primary star. Given the large metallicity uncertainties from PyHammer, we subsequently determine the bulk metallicity of COCONUTS-3A using narrowband spectroscopic features (Section 4.3).

We determine the near-infrared spectral type of COCO-NUTS-3A following Allers & Liu (2013), who derived empirical polynomials between optical spectral types and four H<sub>2</sub>O-band indices using IRTF/SpeX spectra of young and field-age M4-L8 ultracool dwarfs. Allers & Liu (2013) also included a gravity classification system based on the strengths of gravity-sensitive spectral features. We compute an indexbased spectral type of M4.2  $\pm$  0.5 and an intermediate gravity class INT-G (see Section 4.5.8 for further discussion) and caution that such a spectral type is near the margin of the applicable range (M4-L8) for the Allers & Liu (2013) classification. We also measure the H<sub>2</sub>O-K2 index, a spectral type indicator for M0-M9 dwarfs calibrated by Rojas-Ayala et al. (2012), and derive M4.5  $\pm$  1.3. We further compare our SpeX SXD spectrum to M3-M7 spectral standards from the IRTF Spectral Library (Cushing et al. 2005; Rayner et al. 2009) in the J, H, and K bands and assign a visual type of M4.5  $\pm$  0.5 (Figure 4), which we adopt as the final near-infrared spectral type of COCONUTS-3A.

#### 4.3. Metallicity

We compute the bulk metallicity of COCONUTS-3A by using empirical calibrations established using binaries composed of FGK primary stars (with independently measured

[Fe/H]) and M dwarf secondaries. Such M dwarf metallicity calibrations were originally developed for photometry (e.g., Bonfils et al. 2005; Schlaufman & Laughlin 2010; Neves et al. 2012; Johnson et al. 2012) and then extended to moderateresolution spectroscopy ( $R \sim 2000$ ; e.g., Rojas-Ayala et al. 2010, 2012; Terrien et al. 2012; Mann et al. 2013, 2014; Newton et al. 2014). Using a sample of 112 binaries, Mann et al. (2013) derived metallicity calibrations for objects with optical spectral types of K5-M5 using either optical, J-, H-, or K-band spectra as observed by UH 2.2 m/SNIFS or IRTF/ SpeX SXD. They also used their sample to update calibrations in previous work (Lépine et al. 2007; Johnson et al. 2012; Dhital et al. 2012; Terrien et al. 2012). Mann et al. (2014) further extended the calibration to near-infrared spectral types of M4.5–M9.5 using sodium and calcium features in K-band SXD spectra. A metallicity calibration for near-infrared spectral types of M1-M5 was also established by Newton et al. (2014) using the sodium doublet in K-band SXD spectra.

Given that COCONUTS-3A has an optical spectral type of M5.5 and a near-infrared spectral type of M4.5 (Section 4.2), we apply both the Mann et al. (2014) and Newton et al. (2014) calibrations and obtain metallicities of  $0.23 \pm 0.08$  and  $0.16 \pm 0.12$  dex, respectively, with spectral flux uncertainties and calibration errors propagated in a Monte Carlo fashion. We adopt the weighted mean and standard deviation of  $[Fe/H]_{\star} = 0.21 \pm 0.07$  dex as the final metallicity of the COCONUTS-3 system (also see Table 2). Our adopted empirical calibrations were established using field M dwarfs

Table 2
Metallicity and Age of COCONUTS-3A

	Value <sup>a</sup>	Notes
Metallicity	$0.16 \pm 0.12 \text{ dex}$	Newton et al. (2014) calibration (SXD; $R \sim 2000$ )
	$0.23 \pm 0.08 \ dex$	Mann et al. (2014) K-band calibration (SXD)
	$(-0.15 \pm 0.17 \text{ dex})$	Mann et al. (2013) optical-band calibration (SNIFS; $R \sim 1200$ )
	$(0.09 \pm 0.13 \text{ dex})$	Mann et al. (2013) J-band calibration (SXD)
	$(-0.17 \pm 0.11 \text{ dex})$	Mann et al. (2013) H-band calibration (SXD)
	$(0.12 \pm 0.09 \text{ dex})$	Mann et al. (2013) K-band calibration (SXD)
	$(0.11 \pm 0.15 \text{ dex})$	Terrien et al. (2012) H-band calibration as updated by Mann et al. (2013) (SXD)
	$(0.15 \pm 0.14 \text{ dex})$	Terrien et al. (2012) K-band calibration as updated by Mann et al. (2013) (SXD)
Adopted metallicity	$0.21 \pm 0.07 \ dex$	
Stellar activity age	870 <sup>+940</sup> <sub>-570</sub> Myr	$EW_{H\alpha} = -7.18 \pm 0.02 \text{ Å (GMOS; } R \sim 4400)$
	$(2.9^{+2.4}_{-1.4} \text{ Gyr})$	$\mathrm{EW}_{\mathrm{H}\alpha} = -2.9 \pm 0.2 \ \mathrm{\mathring{A}} \ \mathrm{(SNIFS)}$
	≲850 Myr	$\log(L_{\rm X}) = 28.3 \pm 0.2 \text{ dex}, \log(R_{\rm X}) = -2.7 \pm 0.3 \text{ dex}$
	10-750 Myr or older	$\log(F_{\text{NUV}}/F_I) < -3.7 \text{ dex}, \text{NUV} - G > 8.3 \text{ mag}, \text{NUV} - J > 10.1 \text{ mag}$
Kinematics age	≥150 Myr	$UVW = (-34.3 \pm 32.6, -12.1 \pm 48.8, -3.9 \pm 10.7) \text{ km s}^{-1}$
H-R diagram age	100 Myr −1.5 Gyr	$M_G = 11.5826 \pm 0.0015$ mag, BP-RP = $3.088 \pm 0.004$ mag
Lithium age	≥100 Myr	$EW_{Li} < 4 \text{ mA (GMOS)}$
Spectral index age	a few 100 Myr	Na I index = 1.23, Na 8189 index = 0.84, $EW_{Na8200} = 4.50 \text{ Å (GMOS)}$
-	a few 10-100 Myr	$EW_{Na1.138} = 5.6 \pm 0.2 \text{ Å (SXD)}$
Rotation-based age		No rotation period measured from TESS or ASAS-SN
Adopted age	100 Myr −1 Gyr	

#### Note.

with slightly higher surface gravities and older ages than COCONUTS-3A (see Sections 4.5), so we explore the potential surface gravity dependence of our derived  $[Fe/H]_{\star}$  in Appendix A. Based on the PHOENIX stellar models, our bulk metallicity could be underestimated by 0.2–0.3 dex. A more accurate estimate of  $[Fe/H]_{\star}$  would benefit from an empirical calibration customized for young low-mass stars, which is unfortunately not available to date, given that the existing sample of nearby young stars lacks sufficiently large variations in [Fe/H] and mostly has solar metallicity.

While the spectral type of our primary star is just outside the applicable range (K5–M5) of the Mann et al. (2013) calibrations, we applied them to our SNIFS and SpeX SXD spectra and obtained  $[\text{Fe/H}]_{\star} = -0.22 \pm 0.16$  dex in the optical,  $0.09 \pm 0.13$  dex in the J band,  $-0.17 \pm 0.11$  dex in the H band, and  $0.12 \pm 0.09$  dex in the K band. Using the Terrien et al. (2012) H- and K-band calibrations as updated by Mann et al. (2013), we obtain  $[\text{Fe/H}]_{\star} = 0.11 \pm 0.15$  and  $0.15 \pm 0.14$  dex, respectively. Most of these values are  $<1\sigma$  consistent with our adopted metallicity. We find that the spectral features traced by the Mann et al. (2013) optical- and H-band calibrations are not prominent in COCONUTS-3A's spectra, likely leading to less accurate metallicity estimates.

#### 4.4. Physical Properties

We derive the physical properties of COCONUTS-3A using its broadband photometry and empirical relations. We first synthesize its 2MASS and MKO JHK photometry using our SpeX SXD spectra and measure J and  $K_S$  from the VISTA Hemisphere Survey (VHS; McMahon et al. 2013), given that this star lacks MKO photometry, and its 2MASS photometry is contaminated by a diffraction spike from a nearby source. We use the Vega spectrum and obtain 2MASS, MKO, and VHS

filters from Cohen et al. (2003), Hewett et al. (2006), and the ESO VISTA instrument webpage,<sup>6</sup> respectively. We propagate the uncertainties in VHS magnitudes and spectral fluxes in a Monte Carlo fashion, and when the VHS photometry and the synthesized ones are in different bandpasses, we add a 0.05 mag error in quadrature (e.g., Dupuy & Liu 2012). We find that using VHS J and  $K_S$  leads to very similar magnitudes in each band, and we adopt their average and standard deviation as the final synthetic photometry (see Table 1).

Following the empirical calibrations of Mann et al. (2015) and Mann et al. (2019), we convert COCONUTS-3A's  $K_{S,2\text{MASS}}$  absolute magnitude and metallicity into a radius of  $R_{\star} = 0.151 \pm 0.004 \ R_{\odot}$  and mass of  $M_{\star} = 0.123 \pm 0.006 \ M_{\odot}$ leading to a surface gravity of  $\log(g_{\star}) = 5.17 \pm 0.03$  dex. We also compute bolometric luminosity a  $\log(L_{\rm bol,\star}/L_{\odot}) = -2.80 \pm 0.04$  dex by using the Cifuentes et al. (2020) empirical relation between  $L_{bol}$  and  $J_{2MASS}$ -band absolute magnitudes, which is robust over a range of stellar metallicities spanning -1.0 to +0.6 dex (see their Section 4). We then use the Stefan–Boltzmann law to compute an effective temperature of  $T_{\rm eff,\star} = 2966 \pm 85$  K. All measurement uncertainties and calibration errors are propagated in a Monte Carlo fashion.

#### 4.5. Age

#### 4.5.1. Ha Emission

The chromospheric  $H\alpha$  emission probes stellar activity, which is correlated with stellar ages (e.g., Soderblom 2010). Based on  $H\alpha$  measurements of a large M dwarf sample from SDSS, West et al. (2008) noted that the activity fraction of

<sup>&</sup>lt;sup>a</sup> Metallicities inside parentheses are derived from empirical calibrations that are not applicable to COCONUTS-3A's spectral type and have therefore been excluded when computing the final metallicity. Ages inside parentheses are not well constrained and are thereby excluded for determining the final age.

<sup>&</sup>lt;sup>6</sup> http://www.eso.org/sci/facilities/paranal/instruments/vircam/inst/

these objects decreases with vertical distance from the Galactic midplane, and the slope of such a decrease depends on spectral type. Using 1D dynamical simulations encoded with a correlation between stellar ages and Galactic positions, West et al. (2008) derived a model-based activity lifetime for a given M subtype. More recently, an empirical calibration between stellar age and H $\alpha$ -based activity has been established by Kiman et al. (2021) using M dwarfs that are either members of young moving groups or companions to white dwarfs. Kiman et al. (2021) fitted a broken power law to the fractional H $\alpha$  luminosity ( $L_{\rm H}\alpha/L_{\rm bol}$ ) as a function of age and found that  $L_{\rm H}\alpha/L_{\rm bol}$  stays in a saturation regime with a little evolution at <1 Gyr but decreases more rapidly at older ages.

To assess the  ${\rm H}\alpha$  emission of COCONUTS-3A, we measure the equivalent width (EW) using SNIFS and GMOS spectra (with rest-frame vacuum wavelengths) following definitions of the H $\alpha$  line and continuum by Schmidt et al. (2015). We integrate the line flux over 6557.61-6571.61 Å with the pseudocontinuum approximated by the mean flux across two surrounding wavelength regions of 6530-6555 and 6575-6600 Å. We measure  $EW(H\alpha) = -2.9 \pm 0.2$  (SNIFS) and  $-7.18 \pm 0.02$  (GMOS) Å with flux uncertainties propagated in a Monte Carlo fashion. Using slightly different line and continuum definitions by West et al. (2011) and Newton et al. (2017), as well as fitting a Gaussian function for the H $\alpha$  line, we obtain similar EW<sub>H $\alpha$ </sub> values with a <1 Å difference for each spectrum. Therefore, COCONUTS-3A is active, with its  $H\alpha$ emission from the stellar chromosphere rather than disk accretion (e.g., Barrado y Navascués & Martín 2003). We attribute the EW(H $\alpha$ ) difference of 4.3 Å between the SNIFS and GMOS spectra to variability and note that such a strong variability tends to occur for relatively young stars (≤100 Myr; see Figure 7 of Kiman et al. 2021).

We compute  $L_{\rm H\alpha}/L_{\rm bol}=-{\rm EW}({\rm H}\alpha)\times \chi$ , with  $\chi$  being a factor calibrated against broadband colors and spectral types (e.g., Walkowicz et al. 2004; West & Hawley 2008). We use the Douglas et al. (2014) relation between  $\chi$  and optical spectral types and obtain  $\chi=(2.1065\pm0.4167)\times10^{-5}$ , with both the value and error computed as the average of those at M5 and M6 types. We derive  $\log(L_{\rm H\alpha}/L_{\rm bol})=-4.22\pm0.09$  (SNIFS) and  $-3.79\pm0.09$  (GMOS) dex and then estimate the stellar age using the Kiman et al. (2021) H $\alpha$  activity–age relation in a Bayesian framework (also see Zhang et al. 2021b). We evaluate the age (t) based on the following log-likelihood function:

$$\ln \mathcal{L}(t) = -\frac{\left[\log \left(L_{\text{H}\alpha}/L_{\text{bol}}\right)_{\text{model}} - \log \left(L_{\text{H}\alpha}/L_{\text{bol}}\right)_{\text{obs}}\right]^{2}}{2 \times \left(\sigma_{\text{obs}}^{2} + \sigma_{V}^{2}\right)}, (1)$$

where  $\log{(L_{\rm H\alpha}/L_{\rm bol})_{\rm obs}} = -4.22$  (SNIFS) or -3.79 (GMOS), and  $\sigma_{\rm obs} = 0.09$ . We use the best-fit model parameters of Kiman et al. (2021) to compute  $\log{(L_{\rm H\alpha}/L_{\rm bol})_{\rm model}}$  as a function of stellar age (t), with  $\sigma_V = 0.22$  dex. We use the Markov Chain Monte Carlo (MCMC) algorithm *emcee* (Foreman-Mackey et al. 2013) and assume a uniform prior of [1.5 Myr, 10 Gyr] in age. Running MCMC with 20 walkers and 5000 iterations (with the first 100 iterations excluded as burnin), we obtain an age estimate of  $2.9^{+2.4}_{-1.4}$  Gyr and  $870^{+940}_{-570}$  Myr using the SNIFS and GMOS spectra, respectively. Both of these estimates are consistent with the M5 and M6 dwarf model-based activity lifetime of  $<7\pm0.5$  Gyr computed by West et al. (2008).

We caution that the older derived age from the SNIFS spectrum is primarily constrained by a power-law component of the Kiman et al. (2021) models at ages >1 Gyr, which is not well constrained by their very small sample size of six old M dwarfs. Also, the measured  $\log{(L_{\text{H}\alpha}/L_{\text{bol}})_{\text{obs}}} = -4.22 \pm 0.09$  dex from the SNIFS spectrum is in fact consistent with young M dwarfs spanning ages of 10 Myr to 1 Gyr, considering the large scatter in the H $\alpha$  activity–age relation. Therefore, we adopt an H $\alpha$ -based age of  $870^{+940}_{-570}$  Myr as determined from the GMOS spectrum.

#### 4.5.2. X-Ray Emission

As another indicator of stellar magnetic activity, coronal X-ray emission has a qualitatively similar behavior with stellar age as  $H\alpha$  emission. At young ages ( $\lesssim 100$  Myr-1 Gyr), the X-ray-to-bolometric luminosity ratio  $\log(R_{\rm X}) = \log(L_{\rm X}/L_{\rm bol})$  exhibits a plateau, and the specific saturation level tends to increase with lower stellar masses (e.g., Jackson et al. 2012). This plateau is then followed by a power-law decline toward older ages, with a slope weakly dependent on spectral type (e.g., Booth et al. 2017).

To estimate the X-ray emission of COCONUTS-3A, we query the Second ROSAT All-Sky Survey (Boller et al. 2016) using a 30" matching radius and follow Fleming et al. (1995) to convert the measured count rate and hardness ratio (HR1) into a flux  $F_{\rm X} = (1.70 \pm 0.96) \times 10^{-13} {\rm erg \, s^{-1} \, cm^{-2}}$ . Multiple background sources are near the ROSAT X-ray detection, which we find make a negligible contribution to our measured X-ray emission (see Appendix B). We derive an X-ray luminosity of  $log(L_X) = 28.3 \pm 0.2$  dex, similar to M dwarfs in the Pleiades Brandt & Huang 2015) according to Preibisch & Feigelson (2005). Based on Malo et al. (2014), the  $\log(L_X)$  of COCO-NUTS-3A is fainter than that of members of the AB Doradus moving group  $(149^{+51}_{-19} \text{ Myr}; \text{ Bell et al. } 2015)$  and younger associations but brighter than that of the inactive field population. We compute  $log(R_X) = -2.7 \pm 0.3$  dex, suggesting that COCONUTS-3A is in the saturation regime of the X-ray activity-age relation. We also derive flux ratios between the 2MASS J and  $K_S$  $\log(F_{\rm X}/F_{\rm J}) = \log F_{\rm X} + 0.4J + 6.3 = -1.6 \pm 0.2$ and  $\log(F_{\rm X}/F_{K_{\rm S}}) = \log F_{\rm X} + 0.4K_{\rm S} + 7.0 = -1.2 \pm 0.2$ dex, which are comparable with members of the  $\beta$  Pictoris moving group  $(24 \pm 3 \text{ Myr}; \text{ Bell et al. } 2015)$  and the Pleiades (e.g., Shkolnik et al. 2009; Schlieder et al. 2012b). The coronal X-ray activity of COCONUTS-3A thus suggests an age of  $\lesssim$ 850 Myr.

#### 4.5.3. UV Emission

We also study the stellar activity of COCONUTS-3A through UV emission as measured by the Galaxy Evolution Explorer (GALEX; Martin et al. 2005). Using the Mikulski Archive for Space Telescopes, we find that COCONUTS-3A was observed in the near-UV (NUV) band by the GALEX All-Sky Imaging Survey but not detected. We also note that the sources within 1' are all fainter than the GALEX  $5\sigma$  detection limit of 20.5 mag in the NUV. To estimate an upper limit of NUV emission from COCONUTS-3A, we extract all GALEX sources within 10' and exclude problematic photometry with a bright star window reflection, dichroic reflection, detector run proximity, or bright star ghost. We then fit a linear function between these objects' NUV magnitudes and the logarithmic

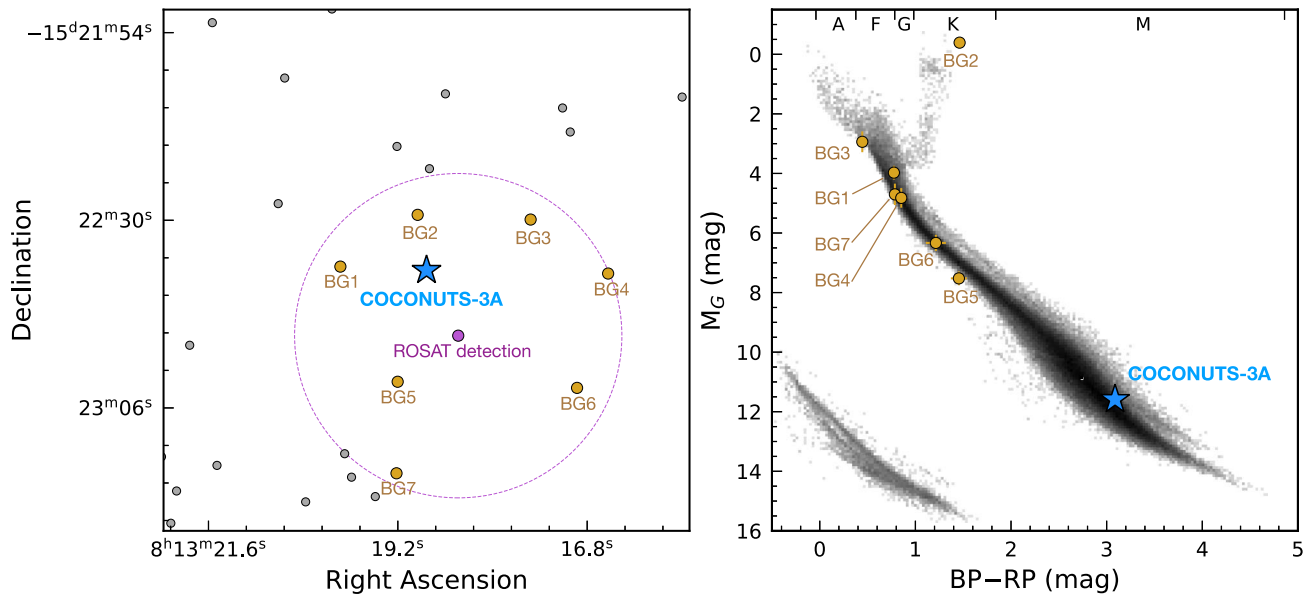


Figure 5. Left: Gaia EDR3 coordinates (at epoch J2000) of COCONUTS-3A (blue) and nearby sources (gray and brown). The seven background stars within 30" (purple dashed circle) of the ROSAT detection 2RXS J081318.4—152252 (purple) are highlighted in brown. Right: Gaia photometry of COCONUTS-3A (blue) and background stars (brown). We also present the number density of Gaia DR2 stars within 100 pc (gray) after applying the photometric and astrometric filters suggested by Appendix B of Gaia Collaboration et al. (2018a).

photometric S/N. We adopt an upper limit of NUV > 22.3 mag, which corresponds to the predicted value at S/N = 2 (e.g., Schneider & Shkolnik 2018).

We compute the flux ratio between the NUV and 2MASS J band as  $\log(F_{\rm NUV}/F_J) = -0.4 \times ({\rm NUV}-J) + 0.358 < -3.7$  dex, as well as colors of NUV -G > 8.3 and NUV -J > 10.1 mag. These upper limits for the NUV emission are broadly consistent with association members spanning ages of 10–750 Myr and older field dwarfs (e.g., Findeisen et al. 2011; Schneider & Shkolnik 2018; Gagné & Faherty 2018).

#### 4.5.4. Kinematics

Combining Gaia EDR3 astrometry and our estimated radial velocity (Section 4.1), we compute the space position and motion of COCONUTS-3A as  $XYZ = (-16.899 \pm 0.011,$  $-25.311 \pm 0.016$ ,  $5.542 \pm 0.004$ ) pc and  $UVW = (-41 \pm 33)$  $-22 \pm 49$ ,  $-2 \pm 11$ ) km s<sup>-1</sup>. Such a space motion is outside but consistent within the uncertainties with the "good box" of young stars as assigned by Zuckerman & Song (2004), with -15 km s<sup>-1</sup>  $\leq U \leq$  0 km s<sup>-1</sup>, -34 km s<sup>-1</sup>  $\leq V \leq$  -10 km s<sup>-1</sup>, and -20 km s<sup>-1</sup>  $\leq W \leq$  +3 km s<sup>-1</sup>. To revisit the ages of objects within the good box, we study the mean space motions of 28 nearby young moving groups from Gagné et al. (2018, 2020). We find that all associations with ages ≥150 Myr have mean space motions outside the good box, while all younger associations fall inside the box, except for IC 2391 (50  $\pm$  5 Myr; Barrado y Navascués et al. 2004), Octans  $(35 \pm 5 \text{ Myr}; \text{ Murphy & Lawson 2015}), \text{ and Taurus } (1-2 \text{ Myr},$ Kenyon & Hartmann (1995); or 1-30 Myr as suggested by, e.g., Kraus et al. 2017; Zhang et al. 2018). We note that the Taurus mean space motion is only  $0.7 \,\mathrm{km \, s^{-1}}$  outside the border. The fact that the mean UVW of COCONUTS-3A is outside the good box suggests it has an age of \$\ge 150\text{ Myr,} although a more precise radial velocity measurement is needed for verification. We also run BANYAN  $\Sigma$  (Gagné et al. 2018) and LACEWING (Riedel et al. 2017), finding

COCONUTS-3A is not associated with any nearby young moving groups.

#### 4.5.5. H-R Diagram Position

According to the MESA isochrones (Paxton et al. 2011; Choi et al. 2016; Dotter 2016), M dwarfs with comparable masses and metallicities to COCONUTS-3A remain in the premain-sequence evolutionary stage for  $\sim 1.5$  Gyr. As shown in Figure 5, COCONUTS-3A is located near the upper envelope of the main sequence, indicating it is younger than a few gigayears. Comparing the Gaia G-band absolute magnitude BP-RP  $(11.5826 \pm 0.0015)$ mag) and  $(3.088 \pm 0.004 \,\mathrm{mag})$  to the empirical isochrones of nearby young moving group members compiled by Kiman et al. (2021), we find that COCONUTS-3A has similar photometry as members of the Pleiades (112  $\pm$  5 Myr), the AB Doradus moving group (149 $^{+51}_{-19}$  Myr), Coma Berenices (562 $^{+98}_{-84}$  Myr; Silaj & Landstreet 2014), Praesepe ( $650 \pm 50 \,\mathrm{Myr}$ ; Douglas et al. 2019), and the Hyades (750  $\pm$  100 Myr) and has a fainter absolute magnitude than younger association members. This suggests an age estimate of 100 Myr-1.5 Gyr.

#### 4.5.6. Lithium Absorption

Approaching the main sequence, young M dwarfs contract and increase their core temperatures, which then burn their initial lithium via convective mixing (e.g., Soderblom 2010). Based on the Chabrier & Baraffe (1997) models, the lithium burning would occur after  $\sim 10$ –15 Myr for M2–M3 dwarfs and  $\sim 100$  Myr for M5–M6 dwarfs (see also Mentuch et al. 2008; Binks & Jeffries 2014, 2016). We measure the EW of lithium EW<sub>Li</sub> for COCONUTS-3A using the GMOS spectrum. To approximate the pseudocontinuum at the lithium absorption feature, we fit a PyHammer template (M6 and [Fe/H] = 0) to the GMOS spectrum, with the scaling factor determined by Equation (2) of Cushing et al. (2008). Both the GMOS and template spectra have vacuum wavelengths in the rest frame,

and we compute EW(Li) over 6708.8–6710.8 Å, leading to an upper limit of 4 mÅ. The absence of lithium absorption in COCONUTS-3A suggests an age of > 100 Myr.

#### 4.5.7. Optical Sodium Doublet

The sodium doublet ( $\lambda\lambda 8183$ , 8195; all wavelengths discussed in this subsection are in the air) is gravity-sensitive and thereby an indicator of stellar age. To quantify the strength of this doublet, Lyo et al. (2004) proposed a Na I index =  $\langle F_{\lambda 8148-8172} \rangle / \langle F_{\lambda 8176-8200} \rangle$ , computed as the ratio between the averaged fluxes over 8148-8172 and 8176-8200 Å. They found that such indices for giant stars are significantly lower than those of higher-gravity main-sequence dwarfs for early-to-mid-M types, with young pre-main-sequence stars falling between these two classes of objects. Riedel et al. (2014) revisited the Na I index with the addition of nearly 50 main-sequence stars and 25 association members, and they cautioned against the interpretation of this index at  $V - K_S \lesssim 5$ mag (\$\leq M3.5). Also, Slesnick et al. (2006a) proposed a Na 8189 index =  $F_{\lambda 8174-8204}/F_{\lambda 8135-8165}$ , defined as the ratio between integrated fluxes over 8174-8204 and 8135-8165 Å. This index is quantitatively equivalent to the inverse of the Lyo et al. (2004) Na I index and is gravity-sensitive, particularly for M2-M7 spectral types (e.g., Slesnick et al. 2006b; Kraus et al. 2017). In addition, Schlieder et al. (2012a) defined an EW of the Na doublet EW<sub>Na8200</sub>, with the absorption line computed from the integrated flux over 8179-8201 Å and the pseudocontinuum approximated by the mean flux over 8149-8169 and 8236-8258 Å. Based on stellar model atmospheres, they suggested that EW<sub>Na8200</sub> can robustly distinguish  $\lesssim$ 100 Myr stars from the field population at  $V - K_S \geqslant 5$  mag.

Here we perform the largest examination of all of these Na spectral indices and EWs by combining the spectra of giant and dwarf stars from the Ultracool RIZzo Spectral Library (Cruz & Gagné 2014) and the Montreal Spectral Library. We make use of all optical and near-infrared spectra that cover the sodium feature and have S/N > 10 at 8190 Å, including 131 giants (K4 -M9), 581 main-sequence field dwarfs (K0-T2), and 56 young dwarfs (M3–L5), which either have  $\beta$ ,  $\gamma$ , or  $\delta$  gravity classes or are kinematic members of ≤200 Myr young moving groups (based on a cross-match with the young moving group census from Gagné et al. 2018 and Gagné & Faherty 2018). We homogeneously determine the Na I index, Na 8189 index, and EW<sub>Na8200</sub> values of these objects, with the spectral flux uncertainties propagated in a Monte Carlo fashion and the vacuum wavelengths of near-infrared spectra put in the air following Ciddor (1996). These spectra were obtained by various instruments that span spectral resolutions of  $R \sim 100-2000$ , with the most common instruments being the Ritchey-Chrétien (504 objects), GoldCam (148 objects), and SpeX (47 objects) spectrographs. Within each data set of giants, main-sequence dwarfs, and young dwarfs, we find that our measured Na indices and EWs exhibit no systematic offsets between the different spectrographs.

Figure 6 presents the Lyo et al. (2004) Na I index, the Slesnick et al. (2006a) Na 8189 index, and the Schlieder et al. (2012a)  $EW_{Na8200}$  as a function of spectral types. We note that the Na doublet strengths of giants and main-sequence dwarfs are distinct, while those of pre-main-sequence dwarfs bridge these two populations with a very large scatter. We also

measure these Na features for COCONUTS-3A using its SNIFS, GMOS, and SpeX SXD spectra and find a <3% discrepancy in a given feature among different spectra. Compared to the library M dwarfs, the strength of COCONUTS-3B's Na doublet  $\lambda\lambda8183,\,8195$  is located near the low-gravity envelope of the main-sequence stars and similar to several young pre-main-sequence M dwarfs with  $\beta$  and  $\gamma$  gravity classes. These suggest an age of a few hundred megayears (e.g., Cruz et al. 2009) but cannot rule out the much older ages given the large scatter of Na indices and EWs of main-sequence stars.

#### 4.5.8. Near-infrared Gravity-sensitive Features

For mid-M to L dwarfs, there are several gravity-sensitive features in the near-infrared (see Allers & Liu 2013 and references therein), including FeH (0.99, 1.20, 1.55  $\mu$ m), VO (1.06  $\mu$ m), Na I (1.138  $\mu$ m), K I (1.169, 1.177, 1.244, 1.253  $\mu$ m), and the shape of the *H*-band continuum (1.46–1.68  $\mu$ m). At a given near-infrared spectral type within M5–L7, Allers & Liu (2013) provided critical values in the EWs or spectral indices of these features, leading to three gravity classes: VL-G (very low gravity), INT-G (intermediate gravity), and FLD-G (field gravity). These gravity classes roughly correspond to ages of  $\lesssim$ 30,  $\approx$ 30–200, and  $\gtrsim$ 200 Myr, respectively, with considerable uncertainties (e.g., Allers & Liu 2013; Liu et al. 2016).

COCONUTS-3A is classified as INT-G based on the Allers & Liu (2013) scheme (see Table 3). Such a gravity class is determined primarily by its low Na I EW at 1.138  $\mu$ m. All of the other gravity-sensitive features cannot be applied to the M4.5 near-infrared spectral type (Section 4.2), but we find that those measured values mostly fall in the low-gravity envelope of the field sequence (also see Artigau et al. 2015) and line up with an INT-G classification. These suggest that COCONUTS-3A likely has an age of  $\approx$ 30–200 Myr but could be younger or older, given its too-early spectral type and the uncertainties in the age–gravity class relation.

#### 4.5.9. Rotation

This object (TIC 125245420) was observed by the Transiting Exoplanet Survey Satellite (TESS) in sectors 7 and 34 with a 30 minute cadence. However, according to Stassun et al. (2019), 83% of the measured flux from the TESS pixels covering COCONUTS-3A is in fact from nearby contaminating sources, especially the close (10") background giant star, which is  $\approx$ 3 mag brighter in the Gaia G band (see Appendix B). The All-Sky Automated Survey for SuperNovae (ASAS-SN; Shappee et al. 2014) provided visible light curves with a cadence of 2–3 days, but its 7."8 pixel scale and  $\sim$ 15" FWHM point-spread function are too large to avoid the contaminating flux from the background giant star.

We also query the Infrared Science Archive to obtain timeseries photometry from DR11 of the Zwicky Transient Facility survey (ZTF; Bellm et al. 2019; Masci et al. 2019) in the *g* and *r* bands (Figure 7). The ZTF images have 1.0 pixels and an FWHM of typically less than 3.0, allowing for COCONUTS-3A and the nearby bright star to be resolved on most nights. Following recommendations in the ZTF Science Data System explanatory supplement, we removed poor-quality detections

https://jgagneastro.com/the-montreal-spectral-library/

<sup>8</sup> http://web.ipac.caltech.edu/staff/fmasci/ztf\_pipelines\_deliverables.pdf

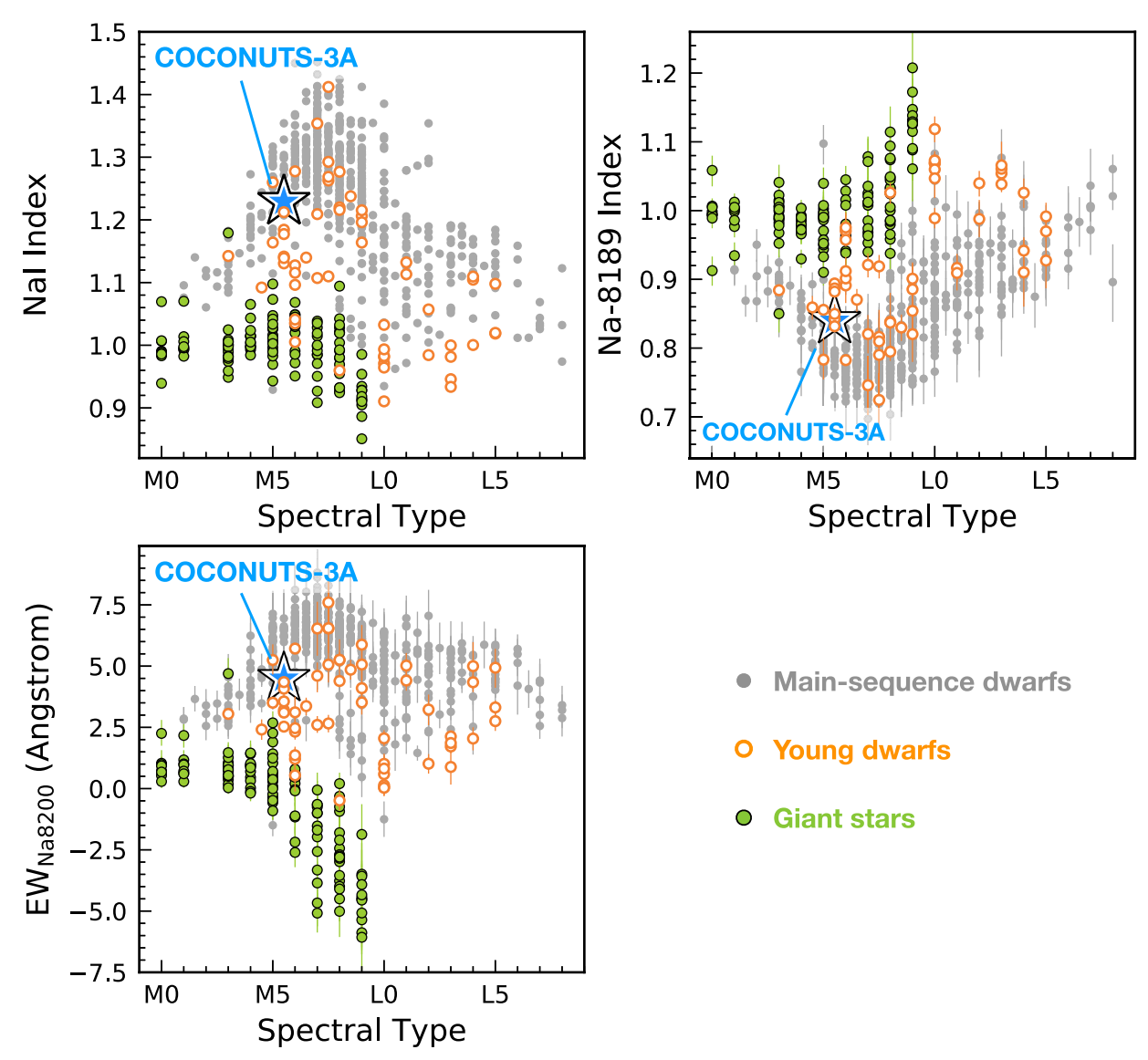


Figure 6. Computed Lyo et al. (2004) Na I index, Slesnick et al. (2006a) Na 8189 index, and Schlieder et al. (2012a) EW<sub>Na8200</sub> of COCONUTS-3A (blue), as well as the main-sequence dwarfs (gray), young dwarfs (orange), and giant stars (green) from the Ultracool RIZzo Spectral Library (Cruz & Gagné, 2014) and the Montreal Spectral Library (Section 4.5.7). These young dwarfs have either  $\beta$ ,  $\gamma$ , or  $\delta$  gravity classes or are kinematic members of  $\lesssim$ 200 Myr young moving groups. Uncertainties are shown if they exceed the symbol size. We note that the strength of the Na doublet of COCONUTS-3A falls in the low-gravity envelope of the main-sequence stars and is similar to several young M dwarfs.

Table 3
Gravity Classification of COCONUTS-3A and 3B Based on the Allers & Liu (2013) System

Spectral Indices	COCONUTS-3A	COCONUTS-3B					
or EWs (Å)	SpeX SXD	SpeX Prism	GNIRS XD				
FeH <sub>z</sub>	$1.053 \pm 0.002$	$1.126^{+0.021}_{-0.023}$	$1.170^{+0.016}_{-0.015}$				
$VO_z$	$0.9902^{+0.0013}_{-0.0012}$	$0.986^{+0.011}_{-0.012}$	$1.004 \pm 0.007$				
$K I_J$	$1.0231^{+0.0011}_{-0.0012}$	$1.030^{+0.009}_{-0.008}$	$1.061 \pm 0.004$				
H-cont	$0.9909^{+0.0010}_{-0.0009}$	$0.895\pm0.008$	$0.906 \pm 0.004$				
Na i 1.138 $\mu \mathrm{m}$	$5.611_{-0.165}^{+0.174}$		$7.464 \pm 0.746$				
K I 1.169 $\mu$ m	•••		$6.616 \pm 0.693$				
K I 1.177 $\mu$ m		•••	$8.042 \pm 0.533$				
K I 1.253 $\mu \mathrm{m}$	$1.435^{+0.124}_{-0.135}$		$4.814 \pm 0.397$				
Gravity class	INT-G	INT-G	INT-G				

from the ZTF light curve by requiring catflags = 1. The resulting light curve has 478 data points (g = 98, r = 380) spanning 1430 days, although 274 of the r-band data come from the 3 hr continuous, deep-drilling observations on 2019 January 11 as part of the high-cadence galactic plane survey (Kupfer et al. 2021). All ZTF images have exposure times of 30 s, and we applied barycentric corrections to the UTC time stamps of each image using the Astropy python package (Astropy Collaboration et al. 2013, 2018).

We do not detect a significant stellar rotation period based on the Lomb–Scargle periodograms derived from the light curves of the combined g and r photometry or the ones of individual bands, likely because the observed time-series photometry is sparsely sampled. Excluding the high-cadence data, the ZTF light curve for COCONUTS-3A has an average observing cadence of 4.7 days. However, the r-band deep-drilling light curve itself exhibits variations that are consistent with a period of  $2.7 \pm 0.2$  hr. This period is very tentative, given that the

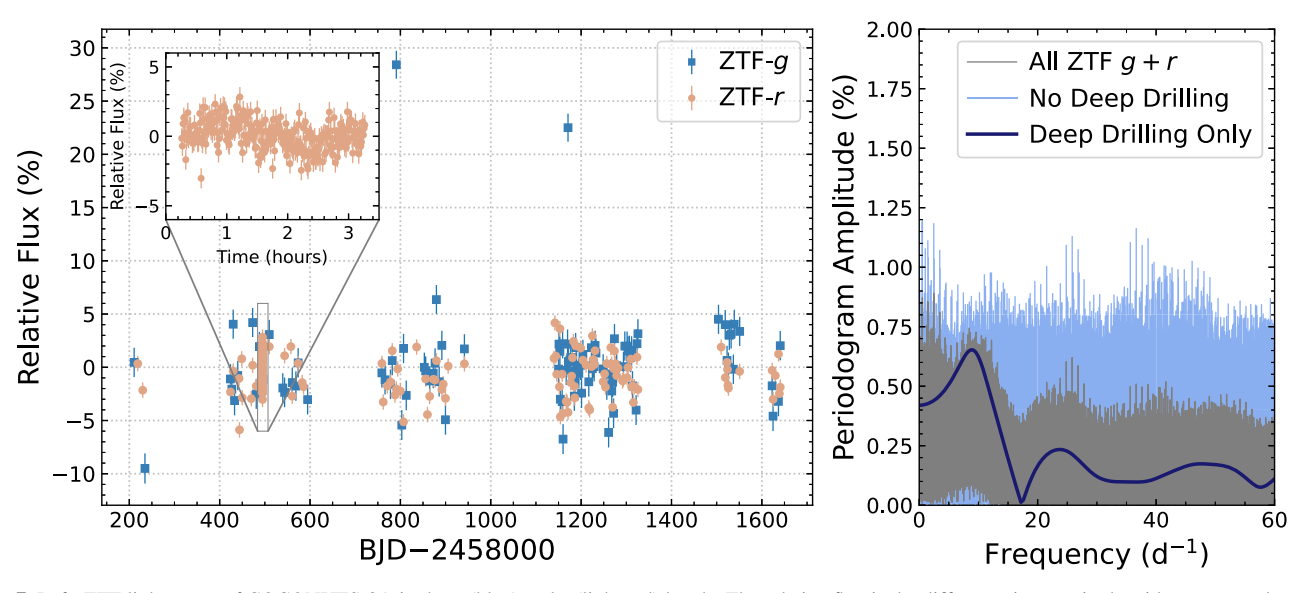


Figure 7. Left: ZTF light curve of COCONUTS-3A in the g (blue) and r (light red) bands. The relative flux is the difference in magnitude with respect to the median magnitude in each band, converted to percentage flux units, while BJD is the barycentric-corrected Julian Date. An inset plot presents a zoom-in view of the high-cadence r-band data taken on 2019 January 11 with a time span of 3 hr. It is unclear if the two bright g-band points are due to flare activity or contamination by the nearby bright source, but regardless, they are ignored during the calculation of the periodograms. Right: periodograms for the ZTF light curve with all combined g and r photometry (gray); the light curve with all but the high-cadence, deep-drilling data (light blue); and the light curve with only high-cadence photometry (dark blue). We detect a tentative period of  $2.7 \pm 0.2$  hr from the r-band deep-drilling light curve and adopt this value as a lower limit for the stellar rotation period of COCONUTS-3A.

Table 4
Spectral Types of COCONUTS-3B Based on the Burgasser et al. (2006) System

Spectroscopy	${ m H_2O}~J$	$\mathrm{CH_4}\ J$	$_{2}$ O $H$	CH <sub>4</sub> H	CH <sub>4</sub> K	Averaged Spectral Type	
SpeX prism $(R \approx 75)$	0.682 (L7.8)	0.902 ( <t0)< td=""><td>0.709 (L6.2)</td><td>1.125 (<t1)< td=""><td>1.006 (L4.2)</td><td>L6.1 ± 1.8</td></t1)<></td></t0)<>	0.709 (L6.2)	1.125 ( <t1)< td=""><td>1.006 (L4.2)</td><td>L6.1 ± 1.8</td></t1)<>	1.006 (L4.2)	L6.1 ± 1.8	
GNIRS XD ( $R \approx 750$ )	0.710 (L7.0)	0.908 ( <t0)< td=""><td>0.703 (L6.4)</td><td>1.118 (<t1)< td=""><td>0.994 (L4.6)</td><td><math display="block">L6.0\pm1.3</math></td></t1)<></td></t0)<>	0.703 (L6.4)	1.118 ( <t1)< td=""><td>0.994 (L4.6)</td><td><math display="block">L6.0\pm1.3</math></td></t1)<>	0.994 (L4.6)	$L6.0\pm1.3$	

entire baseline of the high-cadence light curve is only 3 hr. We therefore place a lower limit of  $P_{\text{rot},\star} \gtrsim 2.7$  hr for COCONUTS-3A, meaning its stellar rotation can be broadly consistent with M dwarfs spanning ages of a few megayears to gigayears (e.g., Rebull et al. 2018).

#### 4.5.10. Age Summary

Table 2 summarizes the age estimates from stellar activity (H $\alpha$ , X-ray, and UV emission), kinematics, photometry, and spectroscopic features. We adopt a final age of 100 Myr-1 Gyr for the COCONUTS-3 system.

### 5. COCONUTS-3B: The Unusually Red L Dwarf Companion

#### 5.1. Spectral Type and Surface Gravity Classification

We first determine the quantitative near-infrared spectral type of COCONUTS-3B using two index-based methods from Burgasser et al. (2006) and Allers & Liu (2013). Burgasser et al. (2006) established a near-infrared classification system for T dwarfs based on five  $\rm H_2O$ - and  $\rm CH_4$ -band features, and Burgasser (2007) later extended this system to spectral types  $\rm LO-T8$  using polynomial fits to these indices. Following this system, we determine a spectral type of  $\rm L6.1\pm1.8$  and  $\rm L6.0\pm1.3$  for COCONUTS-3B based on its SpeX prism and GNIRS XD spectra, respectively, with the uncertainties in the spectral fluxes and polynomial calibrations propagated in an analytic fashion (Table 4).

The Allers & Liu (2013) classification system is based on four  $H_2O$ -band indices and applicable to spectral types of M4 -L8. Only one index ( $H_2OD$ ) provides a reliable classification for >L2 dwarfs, as the other three indices saturate at L2-L8 types (see Figure 6 of Allers & Liu 2013). We determine an  $H_2OD$ -based spectral type of L5.0  $\pm$  0.8 and L5.2  $\pm$  0.7 for COCONUTS-3B using its SpeX and GNIRS spectra, respectively, which are consistent with those derived from the Burgasser et al. (2006) system.

We then derive the Allers & Liu (2013) gravity classification (see Section 4.5.8) of INT-G for both SpeX prism and GNIRS XD spectra. The derived gravity class lines up with the moderately young age of the primary star COCONUTS-3A (Section 4.5). While field-age, dusty L dwarfs can have similar spectral slopes as their young, low-gravity counterparts (e.g., Looper et al. 2008; Kirkpatrick et al. 2010; also see Figure 8), the Allers & Liu (2013) gravity classification system can effectively distinguish these two classes of objects. Indeed, we find that the FeH<sub>z</sub> index and K I EWs of COCONUTS-3B are distinct from those of high-gravity, dusty L dwarfs with similar spectral types (see Figures 20 and 23 of Allers & Liu 2013).

In Figures 8 and 9, we determine the visual spectral type and gravity class of COCONUTS-3B by comparing its SpeX prism and GNIRS XD data to the following spectral standards:

(1) L5–L8 FLD-G dwarfs (Kirkpatrick et al. 1999; Cruz et al. 2003; Cushing et al. 2005; Chiu et al. 2006; Rayner et al. 2009; Burgasser et al. 2010);

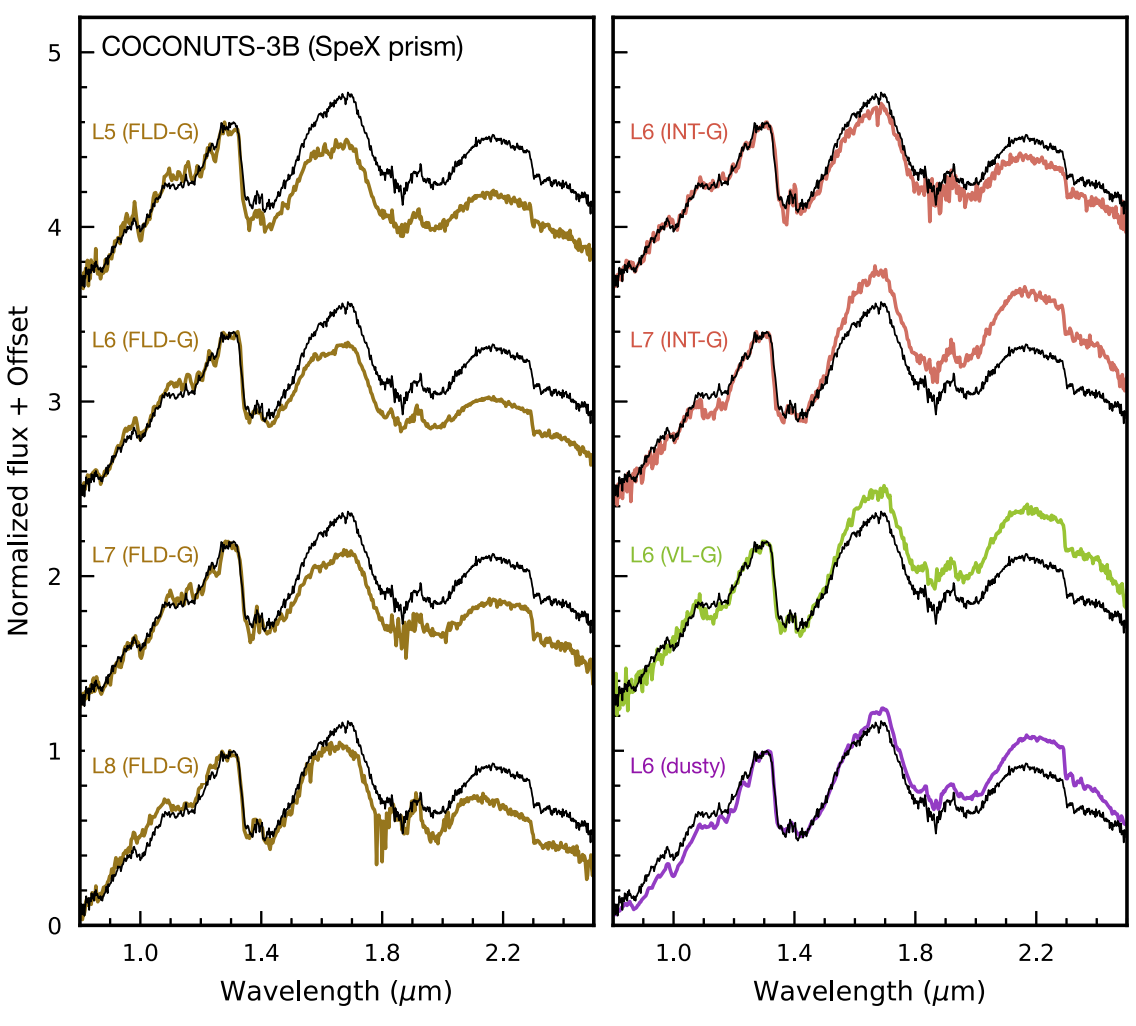


Figure 8. Left: SpeX prism spectrum of COCONUTS-3B (black) compared to L5–L8 spectral standards (brown) from the SpeX Prism Library (Burgasser 2014): 2MASS J08350622+1953050 (L5; Chiu et al. 2006), 2MASS J10101480-0406499 (L6; Cruz et al. 2003), 2MASS J0028208+224905 (L7; Burgasser et al. 2010), and 2MASS J16322911+1904407 (L8; Kirkpatrick et al. 1999). All of these standards have an FLD-G gravity class. In the right panel, we also compare COCONUTS-3B's spectrum to the SpeX prism spectra of an L6 INT-G dwarf, 2MASSI J0103320+193536 (2MASS J0103+1935; red; Cruz et al. 2004); an L7 INT-G dwarf, WISEP J004701.06+680352.1 (WISE J0047+6803; red; Gizis et al. 2012, 2015); an L6 VL-G dwarf, 2MASSW J2244316+204343 (2MASS J2244+2043; green; Looper et al. 2008); and a dusty, unusually red L6 FLD-G dwarf, 2MASS J21481628+4003593 (2MASS J2148+4003; purple; Looper et al. 2008). All spectra shown in this figure are normalized by their *J*-band peak fluxes. The spectrum of COCONUTS-3B is best matched by that of 2MASS J0103+1935, leading to a visual spectral type of L6 INT-G.

- (2) an L6 INT-G dwarf, 2MASSI J0103320+193536 (2MASS J0103+1935; McLean et al. 2003; Cruz et al. 2004);
- (3) an L7 INT-G dwarf, WISEP J004701.06+680352.1 (WISE J0047+6803; Gizis et al. 2012, 2015);
- (4) an L6 VL-G dwarf, 2MASSW J2244316+204343 (2MASS J2244+2043; Looper et al. 2008); and
- (5) an L6 FLD-G dwarf with a dusty atmosphere and unusually red colors, 2MASS J21481628+4003593 (2MASS J2148+4003; Looper et al. 2008).

The spectra of COCONUTS-3B are best matched by those of 2MASS 0103+1935, suggesting a visual classification of L6 INT-G.

Schneider et al. (2017) determined a near-infrared spectral type of L7 for COCONUTS-3B by comparing this object's CTIO/ARCoIRIS spectra to the Kirkpatrick et al. (2010) spectral standards based on  $\chi^2$  values. Their derived spectral type was based on the best match, 2MASS 0103+1935, which had an L7 spectral type initially assigned by Kirkpatrick et al. (2010) but then became the L6 INT-G standard later suggested

by Allers & Liu (2013). The Schneider et al. (2017) spectral type is therefore the same as our visual classification result.

Cruz et al. (2018) suggested that 2MASS 0103+1935 has no low-gravity spectral features in the optical wavelengths and thus might not be an appropriate L6 INT-G standard. This will only impact our visual gravity classification of COCONUTS-3B, but the low surface gravity of our companion is also supported by the quantitative spectral indices and EWs of its gravity-sensitive features based on Allers & Liu (2013), its very red near-infrared colors, and the moderately young age of COCONUTS-3A.

Combining our index-based and visual spectral classification, we adopt an L6  $\pm$  1 INT-G as the final near-infrared spectral type for COCONUTS-3B.

#### 5.2. Bolometric Luminosity and Synthesized Photometry

We determine the bolometric luminosity of COCONUTS-3B by integrating its spectral energy distribution (SED). We first flux-calibrate both the SpeX prism and GNIRS XD spectra of the companion using its observed VHS  $K_S$  magnitude. Then we

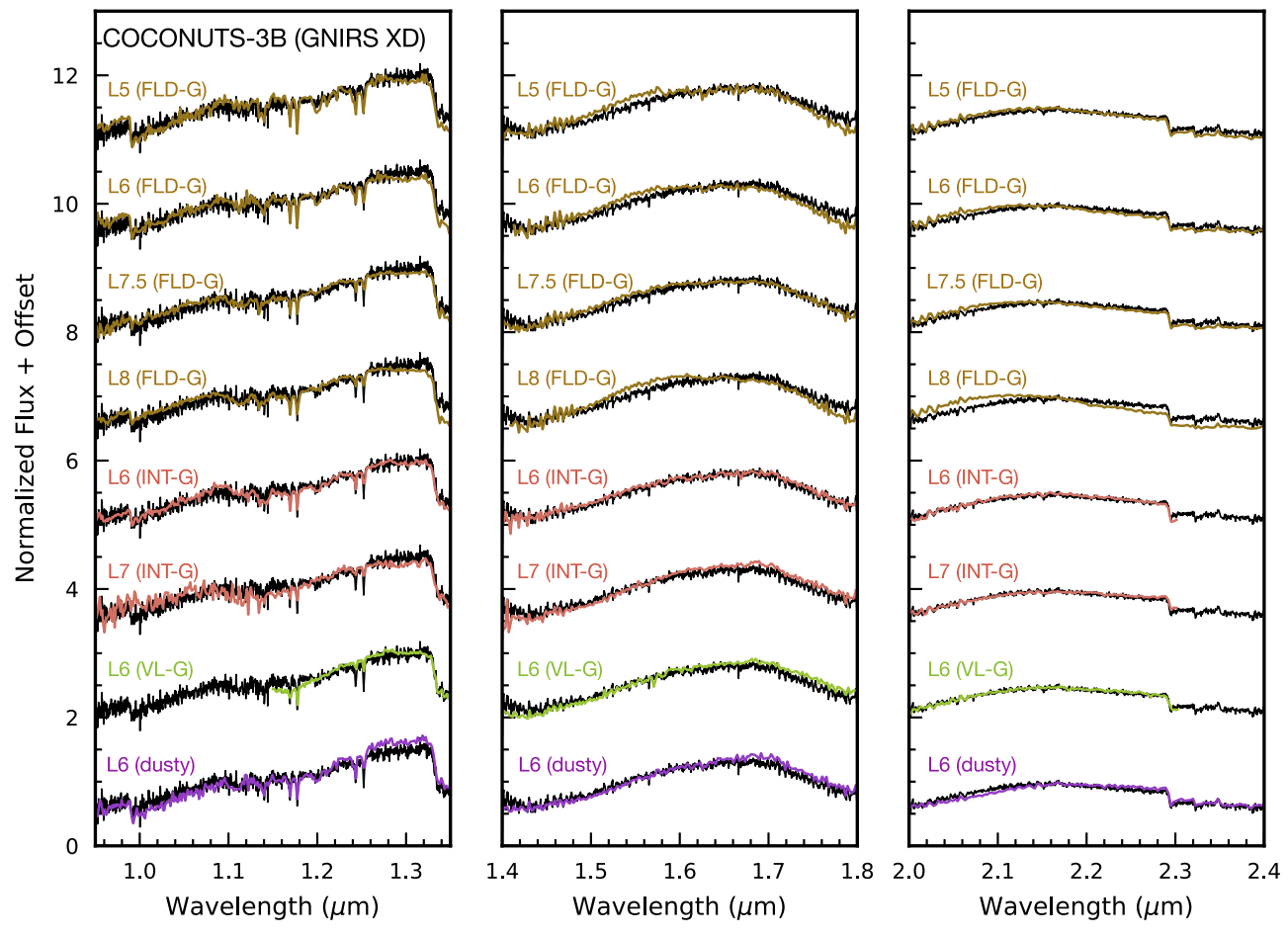


Figure 9. The GNIRS XD spectrum of COCONUTS-3B (black) compared to the SpeX SXD spectra ( $R \sim 2000$ ) of L5–L8 standards from the IRTF Spectral Library (Cushing et al. 2005; Rayner et al. 2009) in the J, H, and K bands (brown): 2MASS J15074769–1627386 (L5 FLD-G), 2MASS J15150083+4847416 (L6 FLD-G), 2MASS J08251968+2115521 (L7.5 FLD-G), and DENIS-P 025503.3–470049.0 (L8 FLD-G). We also include the moderate-resolution spectra ( $R \sim 2000$ ) of 2MASS J0103+1935 (L6 INT-G; red; Keck/NIRSPEC data by McLean et al. 2003), WISE J0047+6803 (L7 INT-G; red; SpeX SXD data by Gizis et al. 2015), 2MASS J2244+2043 (L6 VL-G; green; NIRSPEC data by McLean et al. 2003), and 2MASS J2148+4003 (purple; SpeX SXD data by Looper et al. 2008), whose low-resolution spectra are in Figure 8. We have downgraded the spectral resolution of all standards to match that of the GNIRS XD data ( $R \sim 750$ ) and normalized all spectra by their average fluxes in each band. The L6 INT-G standard 2MASS J0103+1935 provides the best match to COCONUTS-3B.

construct an SED by combining the object's  $0.9-2.4~\mu m$  SpeX prism spectrum with broadband fluxes from  $z_{P1}$  and CatWISE W1 and W2 photometry. We linearly interpolate the fluxes to fill in the wavelength gaps between the spectra and broadband fluxes. At shorter wavelengths than  $z_{P1}$ , we linearly extrapolate the SED to zero flux at zero wavelength, and at longer wavelengths beyond W2 (with a cut at  $1000~\mu m$ ), we append a Rayleigh–Jeans tail. We compute the bolometric luminosity of  $\log(L_{\rm bol}/L_{\odot}) = -4.451 \pm 0.002$  dex, with the uncertainties of the SED fluxes and the host star's parallax propagated in a Monte Carlo fashion. We also construct the SED using the companion's GNIRS XD data with wavelengths of 0.95-1.35, 1.45-1.8, and  $1.95-2.4~\mu m$  to avoid spectra with low S/Ns and significant telluric features. Integrating this GNIRS-based SED leads to a consistent  $L_{\rm bol}$  with the SpeX-based value within  $1\sigma$ .

To examine the systematic error of our computed  $L_{\rm bol}$ , we apply the same SED analysis to a set of Saumon & Marley (2008) atmospheric model spectra whose fluxes are scaled at the substellar surface, spanning  $T_{\rm eff} = 1000-1600$  K (100 K intervals),  $\log(g) = 4$  and 5 dex, and  $f_{\rm SED} = 1$  and 2. These physical parameters are close to the properties of COCONUTS-3B (see Sections 5.3 and 5.4). We synthesize  $z_{\rm Pl}$ , W1, and W2 broadband fluxes for each model spectrum, and then we tailor

the spectral resolution and wavelength range of the models to match those of our SpeX and GNIRS data used for the aforementioned SED construction. We also conduct the same linear interpolation and extrapolation to generate model-based SED fluxes spanning  $0-1000 \mu m$ . By integrating our emulated SED at each model grid point, we compute the bolometric flux  $F_{\rm bol}$  and then compare with the original model value of  $F_{\rm bol,true} = \sigma T_{\rm eff}^4$ , where  $\sigma$  is the Stefan-Boltzmann constant. Among all grid points, we find that the mean and standard deviation of  $\log(F_{\text{bol,true}}) - \log(F_{\text{bol}})$  is  $-0.003 \pm 0.033$  dex for SpeX-based SEDs and  $-0.010 \pm 0.033$  dex for GNIRS-based SEDs. These differences in logarithmic bolometric fluxes between the computed values from emulated SEDs and the original values equal the differences in logarithmic bolometric luminosities. We therefore adopt a systematic error of 0.03 dex for our SED-based  $L_{bol}$  and derive a bolometric luminosity of  $\log(L_{\rm bol}/L_{\odot}) = -4.45 \pm 0.03$  dex for COCONUTS-3B.

We also synthesize 2MASS and MKO magnitudes for COCONUTS-3B using its spectra and VHS photometry following Section 4.4. For each broadband X in  $\{J_{2MASS}, H_{2MASS}, K_{S,2MASS}, Y_{MKO}, J_{MKO}, H_{MKO}, K_{MKO}\}$ , we use each of the companion's SpeX prism and GNIRS XD spectra to compute two colors, X-J and  $X-K_S$ , with the J and  $K_S$ 

bands from VHS. Spectral flux uncertainties are propagated into these computed colors in a Monte Carlo fashion. For this calculation, we use the Vega spectrum and obtain 2MASS, MKO, and VHS filters from Cohen et al. (2003), Hewett et al. (2006), and the ESO VISTA instrument webpage (see Section 4.4), respectively. We thus obtain four estimates of the *X*-band magnitude by computing J + (X - J) and  $K_S + (X - K_S)$  using the SpeX and GNIRS spectra. We confirm that all four of these estimates in a given band *X* are consistent within  $1\sigma$  and compute their average and the standard deviation. For *X* that is not *J* or *K* band, we follow Dupuy & Liu (2012) and incorporate an additional 0.05 mag systematic error to the final synthetic photometry (see Table 1).

We find that our synthesized  $H_{2\text{MASS}} = 15.89 \pm 0.06$  mag is brighter than the observed  $H_{2\text{MASS}} = 16.25 \pm 0.18$  mag by 0.36 mag (2.0 $\sigma$ ), and our synthesized  $K_{S,2MASS} = 15.02 \pm 0.03$ mag is fainter than the observed  $K_{S,2\text{MASS}} = 14.86 \pm 0.13$  mag by  $0.16 \,\mathrm{mag}$   $(1.2\sigma)$ . These indicate that the observed  $H_{2\text{MASS}} - K_{S,2\text{MASS}}$  is  $\sim 0.5$  mag redder than the color from our SpeX prism and GNIRS XD data, although these two spectra have consistent morphology and do not exhibit noticeable spectral variability. In addition, if we compute the VHS  $J - K_S$  color using our SpeX and GNIRS spectra, then these values are both consistent with the observed  $J - K_S$  color within 0.05 mag. The observed  $H_{2\text{MASS}}$  and  $K_{5,2\text{MASS}}$  magnitudes of COCONUTS-3B are not blended or affected by artifacts but have modest S/Ns ( $\approx$ 5–8). We therefore recommend using our synthetic photometry in the 2MASS bands. Photometric variability monitoring of this object will be valuable to investigate this discrepancy.

We compute the photometric distance of COCONUTS-3B as  $32\pm7$  pc by using its synthetic  $J_{\rm MKO}$  magnitude and the typical  $J_{\rm MKO}$ -band absolute magnitude of L6 INT-G dwarfs provided by Table 10 of Liu et al. (2016). As discussed in Section 2, this distance for COCONUTS-3B is consistent with that of COCONUTS-3A ( $d=30.88\pm0.02$  pc) and validates their physical association.

#### 5.3. Physical Properties Based on Evolution Models

We infer COCONUTS-3B's effective temperature  $(T_{\rm eff})$ , surface gravity  $(\log(g))$ , radius (R), and mass (M) by using the hot-start Saumon & Marley (2008) cloudy evolutionary models. These models parameterize the sedimentation efficiency of condensate particles via  $f_{\rm SED}$  using the Ackerman & Marley (2001) framework and include a grid of  $f_{\rm SED}=1, 2, 3, 4$ , with a higher  $f_{\rm SED}$  meaning a larger average cloud particle size and higher sedimentation efficiency and thereby less cloud effect on the photosphere. To reproduce the photometric sequence of MLT-type ultracool dwarfs, Saumon & Marley (2008) also produced a suite of "hybrid" models with  $f_{\rm SED}=1$  for  $T_{\rm eff}\geqslant 1400$  K and  $f_{\rm SED}=4$  for  $T_{\rm eff}\leqslant 1200$  K. For 1200 K <  $T_{\rm eff}<1400$  K, they interpolated the surface boundary condition in  $T_{\rm eff}$  using the  $f_{\rm SED}=2$  models at  $T_{\rm eff}=1400$  K and the cloudless models at  $T_{\rm eff}=1200$  K.

We assume that COCONUTS-3B's age follows a uniform distribution spanning [0.1, 1.0] Gyr (Section 4.5) and its  $\log(L_{\rm bol}/L_{\odot})$  follows a normal distribution of  $N(\mu=-4.45,\,\sigma^2=0.03^2)$ . We draw random age and  $\log(L_{\rm bol}/L_{\odot})$  values from these distributions to linearly interpolate the grid of physical parameters predicted by the Saumon & Marley (2008) hybrid evolution models at these ages and  $\log(L_{\rm bol}/L_{\odot})$ . Such interpolation is conducted logarithmically for the  $T_{\rm eff}$  values.

Computing the median and 16th-to-84th percentile intervals of the interpolated model parameters, we derive  $T_{\rm eff} = 1362^{+48}_{-73}$  K,  $\log(g) = 4.96^{+0.15}_{-0.34}$  dex,  $R = 1.03^{+0.12}_{-0.06}$   $R_{\rm Jup}$ , and  $M = 39^{+11}_{-18}$   $M_{\rm Jup}$  as the evolution-based physical properties of COCONUTS-3B.

Our derived physical properties will inevitably carry any systematic errors in the evolution model predictions. Dupuy et al. (2009, 2014) measured the dynamical masses of two binaries composed of mid-L brown dwarfs, HD 130948BC (L4 +L4) and Gl417BC (L4.5+L6) based on orbit monitoring. These two binaries are both companions to solar-mass host stars and thus have independently known ages. Similar to our analysis of COCONUTS-3B, Dupuy et al. used these L dwarfs' ages and observed bolometric luminosities to infer their masses from several evolution models. However, they found that the evolution-based masses are higher than their directly measured values by ≈25% for the Saumon & Marley (2008) hybrid evolution models. Recently, Brandt et al. (2019, 2021) further expanded the dynamical mass sample by combining radial velocities, relative astrometry, and the Hipparcos-Gaia accelerations of several systems hosting brown dwarf companions, including three L dwarfs, HR 7672B (L4.5; Liu et al. 2002), HD 33632Ab (L9.5 $^{+1.0}_{-3.0}$ ; Currie et al. 2020), and HD 72946B (L5.0  $\pm$  1.5; Maire et al. 2020). These objects' masses predicted by Saumon & Marley (2008) hybrid evolution models given their ages and  $L_{bol}$  are all consistent with their dynamical masses, although these L dwarfs have older ages  $(\approx 2 \text{ Gyr})$  than HD 130948BC and Gl 417BC ( $\approx 800 \text{ Myr}$ ). If the evolution-based properties of COCONUTS-3B suffer from the same systematic errors as HD 130948BC and Gl 417BC, then its true mass might be as low as  $\sim 30 M_{\text{Jup}}$ .

In addition, we note that our derived physical properties of COCONUTS-3B are based on solar-metallicity evolution models, while its host star has a slightly supersolar bulk metallicity (Section 4.3). To estimate this metallicity effect, we recompute the physical properties of COCONUTS-3B using two classes of the cloudless Saumon & Marley (2008) evolution models with [Fe/H] = 0 and +0.3 dex. Switching models from solar to a supersolar metallicity, COCONUTS-3B will have a 21 K cooler  $T_{\rm eff}$ , a 0.04 dex lower  $\log(g)$ , a 0.03  $R_{\rm Jup}$  larger R, and a 2  $M_{\rm Jup}$  smaller M. These systematic differences are all much smaller than the uncertainties of our derived properties.

#### 5.4. Discussion

5.4.1. Comparison with Saumon & Marley (2008) Atmospheric Model Spectra

To examine whether the Saumon & Marley (2008) models can sufficiently interpret the atmospheres of mid-to-late-L dwarfs like COCONUTS-3B, we construct the Saumon & Marley (2008) atmospheric model spectra at this companion's evolution-based physical properties. Specifically, we linearly interpolate the model spectra using the distributions of  $T_{\rm eff}$  and  $\log(g)$  computed in Section 5.3 and then scale these models by the companion's evolution-based R and COCONUTS-3A's parallax. As demonstrated in Zhang et al. (2020, 2021c), the difference between these evolution-based model spectra and the objects' observed spectra can reveal the shortcomings of the assumptions adopted by model atmospheres.

Figure 10 compares the SpeX prism spectrum and broadband fluxes of COCONUTS-3B to the evolution-based Saumon &

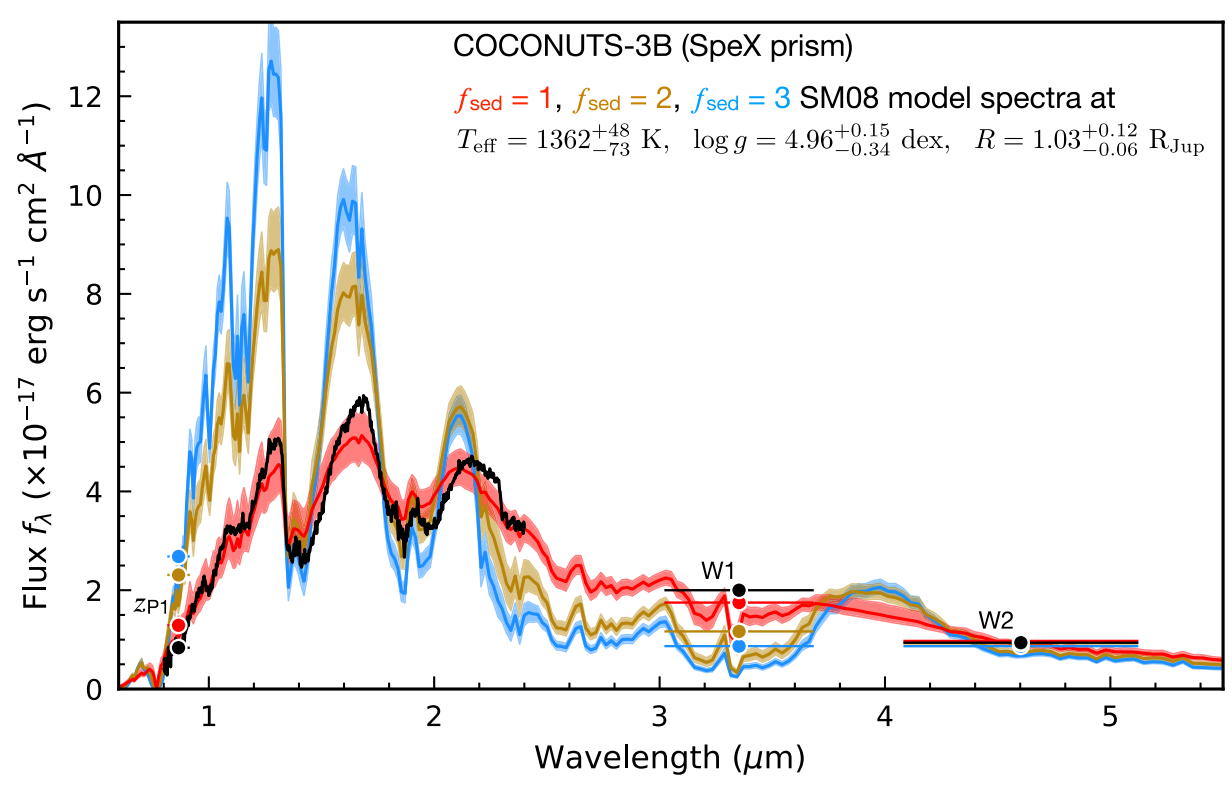


Figure 10. SpeX prism spectrum of COCONUTS-3B (black) compared to the evolution-based Saumon & Marley (2008) model spectra described in Section 5.4.1, with  $f_{\rm SED}=1,2,3$  models displayed in red, brown, and blue, respectively. We use colored solid lines and shading to present the median and 68% confidence intervals of the model spectra constructed at the evolution-based  $T_{\rm eff}$ ,  $\log(g)$ , and R of COCONUTS-3B. We also synthesize  $z_{\rm Pl}$ , W1, and W2 fluxes using these models (colored circles) and compare them with the observed photometry (black circles). The SED of COCONUTS-3B can be best matched by atmospheric models with  $f_{\rm SED}=1$ , suggesting that the companion retains ample condensate clouds in its photosphere.

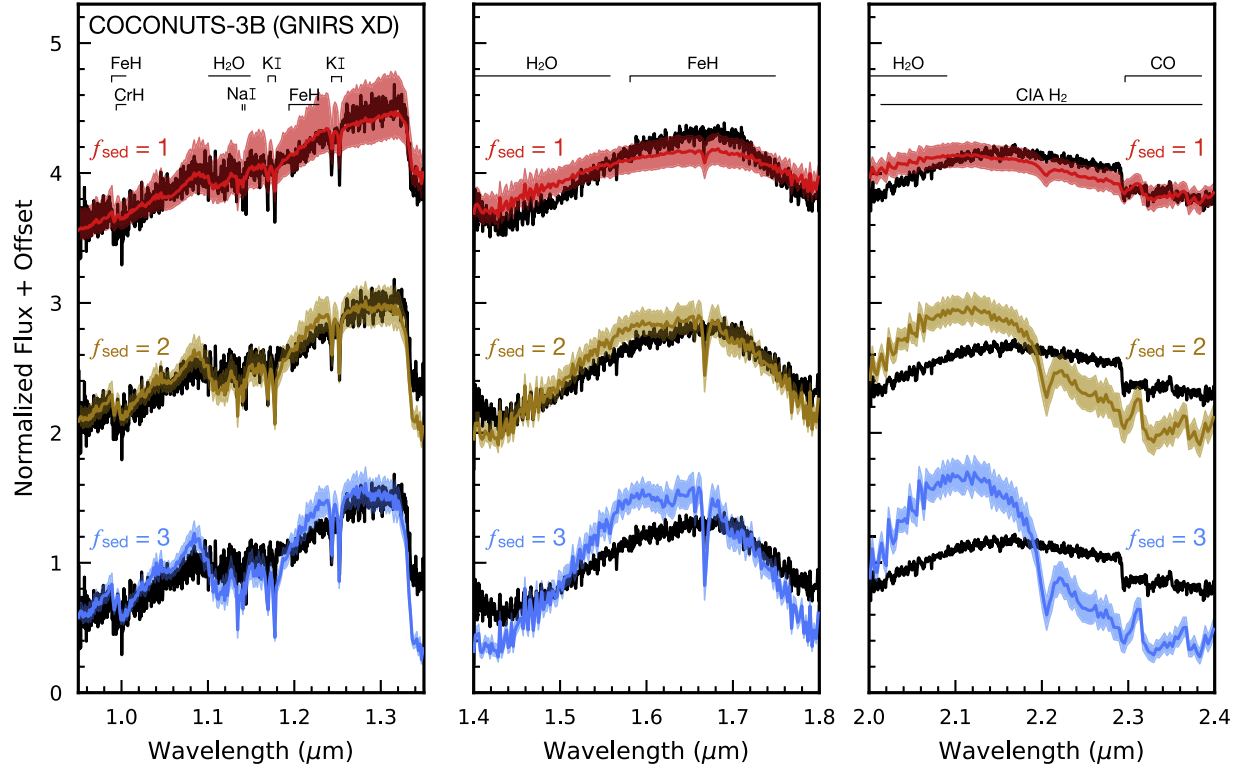


Figure 11. The GNIRS XD spectrum of COCONUTS-3B (black) compared to the evolution-based Saumon & Marley (2008) model spectra (colored; same as in Figure 10) in individual *JHK* bands. All spectra are normalized by their mean values within each band. The data are best matched by  $f_{\rm SED} = 1$  models, although these models predict too-shallow depths in the Na I and K I resonance lines in the *J* band and a slightly bluer spectral slope in the *K* band than the observation. The absorption feature at  $\sim 1.66 \ \mu m$  predicted by the models is likely due to the incomplete CH<sub>4</sub> line list used by the Saumon & Marley (2008) models.

Marley (2008) model spectra with  $f_{SED} = 1, 2, 3$ . Figure 11 further examines the moderate-resolution spectral features by comparing these models to the GNIRS XD data. The spectrophotometry of COCONUTS-3B is best described by dusty atmospheres with  $f_{SED} = 1$ , although such models produce slightly brighter  $z_{P1}$ -band and fainter W1-band fluxes than the observed values. Also, these  $f_{\text{SED}} = 1$  models predict tooshallow depths for the Na I and K I resonance lines in the J band and a slightly bluer K-band spectral slope than the data. These differences are very likely due to the older version of the opacity database (e.g., Freedman et al. 2008) for the alkali lines (in the red optical and J bands),  $CH_4$  (in the H, K, and W1bands), and collision-induced  $H_2$  absorption (in the K band) adopted by Saumon & Marley (2008). New sets of cloudy models that incorporate the updated opacities (e.g., Saumon et al. 2012; Yurchenko et al. 2013; Yurchenko & Tennyson 2014; Ryabchikova et al. 2015; Allard et al. 2016, 2019) will likely improve the consistency between model predictions and observations, leading to more reliable estimates of these objects' physical properties via atmospheric modeling.

#### 5.4.2. Comparison with Previously Known Ultracool Benchmarks

To place our discovery in context, we compare the photometry of COCONUTS-3B to that of the L6-Y1 benchmarks compiled by Zhang et al. (2020, 2021a) in Figure 12. These benchmarks include wide-orbit comoving companions to stars, kinematic members of nearby young moving groups, and components of substellar binaries with dynamical masses. All of these objects have independently known ages or masses that are usually impossible to determine for free-floating single brown dwarfs in the field. We also compare the *J*-band absolute magnitude and J-K color of COCONUTS-3B to the photometric sequences of FLD-G, INT-G, and VL-G ultracool dwarfs from Liu et al. (2016). COCONUTS-3B has slightly brighter and bluer near-infrared photometry than the L6 VL-G objects but is much fainter and redder than their FLD-G counterparts. Also, the  $J_{\rm MKO}-K_{\rm MKO}=2.11\pm0.02$  mag of COCONUTS-3B is among the reddest of all ultracool benchmarks with ages older than a few hundred megayears. COCONUTS-3B is in fact similar to the brown dwarf companion HD 206893B, which has a moderately young age (50–700 Myr based on its host star) and an extremely red nearinfrared color (Delorme et al. 2017; Milli et al. 2017).

Field-age, high-gravity L6 dwarfs have a typical  $\log(L_{\rm bol}/L_{\odot})$  of  $-4.37\pm0.14$  dex and a  $T_{\rm eff}$  of  $1483\pm113$  K based on polynomial fits in Zhang et al. (2020) and Filippazzo et al. (2015), respectively. COCONUTS-3B has a 0.08 dex (0.5 $\sigma$ ) fainter bolometric luminosity and 121 K (1.0 $\sigma$ ) cooler effective temperature compared to its high-gravity counterparts with similar spectral types. The companion's lower  $T_{\rm eff}$ , faint absolute magnitude, and red colors are in accord with its moderately young age, intermediate surface gravity, and dusty atmospheres, given that the properties of L/T transition objects

are known to be surface gravity-dependent (e.g., Metchev & Hillenbrand 2006; Marley et al. 2012; Liu et al. 2016; Faherty et al. 2016).

#### 5.4.3. Formation Scenario

Formation of planetary-mass and substellar companions that reside on very wide orbits (a few 100–1000 au) is intriguing. These companions might form in situ like components of stellar binaries via fragmentation of the collapsing protostellar clouds (e.g., Kroupa 2001; Chabrier 2003). Alternatively, they might form like closer-in exoplanets via core/pebble accretion or disk gravitational instability and then scatter outward to large orbital separations due to dynamical interactions with other system components (e.g., Boss 2006; Veras et al. 2009). For the COCONUTS-3 system, it is very likely that the companion formed in a starlike fashion, given that the companion's mass of  $\approx$ 40  $M_{\rm Jup}$  is  $\gtrsim$ 10× larger than the expected total mass of protoplanetary disks surrounding low-mass ( $\approx 0.1 M_{\odot}$ ) M dwarfs like COCONUTS-3A (e.g., Ansdell et al. 2016; Pascucci et al. 2016; Manara et al. 2018). In addition, a companion-to-host mass ratio of  $0.29 \pm 0.10$  for the COCO-NUTS-3 system is much higher than those of directly imaged exoplanets ( $\leq 0.04$ ; e.g., Marois et al. 2008, 2010; Macintosh et al. 2015; Bohn et al. 2020, 2021; also see Figure 3 of Zhang et al. 2021b).

#### 6. Conclusion

We have reported the third discovery from our COol Companions ON Ultrawide orbiTS (COCONUTS) program. The COCONUTS-3 system is composed of a young M dwarf primary star with strong H $\alpha$  and X-ray emission, as well as an unusually red L dwarf companion that was previously identified as the free-floating object WISEA J081322.19 -152203.2 by Schneider et al. (2017). Given the consistency in proper motions and distances, we confirm the physical association between the A and B components and compute a projected separation of 61" (1891 au). Based on the primary star's optical and near-infrared spectrophotometry, we derive its physical properties (e.g.,  $T_{\rm eff,\star} = 3291 \pm 49$  K and  $M_{\star} = 0.123 \pm 0.006 M_{\odot}$ ) and a slightly supersolar metallicity of  $[Fe/H]_{\star} = 0.21 \pm 0.07$  dex. We note that this  $[Fe/H]_{\star}$  is derived using empirical calibrations established by older and higher-gravity M dwarfs and could be underestimated by 0.2-0.3 dex according to PHOENIX stellar models given COCONUTS-3A's younger age and lower surface gravity. Combining the host star's stellar activity, kinematics, H-R diagram position, lithium absorption, and surface gravity-sensitive spectroscopic features, we estimate an age of 100 Myr to 1 Gyr for the COCONUTS-3 system.

We also study the near-infrared spectra of COCONUTS-3B and derive a spectral type of L6 with an intermediate surface gravity classification (INT-G). Based on the companion's observed bolometric luminosity and its host star's age, we use the hot-start Saumon & Marley (2008) hybrid evolution models to infer the physical properties of COCONUTS-3B to be  $T_{\rm eff} = 1362^{+48}_{-73}$  K,  $\log(g) = 4.96^{+0.15}_{-0.34}$  dex,  $R = 1.03^{+0.12}_{-0.06}$   $R_{\rm Jup}$ , and  $M = 39^{+11}_{-18}$   $M_{\rm Jup}$ . It has been recently suggested that the ultracool evolution models tend to overpredict the mass at a given  $L_{\rm bol}$  and age by  $\sim 25\%$  for moderately young brown dwarfs (<1 Gyr) based on two substellar binary systems with

Delorme et al. (2017) synthesized HD 206893B's  $J_S$ -band magnitude from their VLT/SPHERE IFS spectroscopy ( $R \sim 30$ ) with S/N  $\approx 10$  and measured K1- and K2-band magnitudes using IRDIS data, leading to very red colors of  $J_S - K1 = 3.13 \pm 0.20$  and  $J_S - K2 = 3.45 \pm 0.19$  mag. We synthesize  $J_S - K1 = 1.969 \pm 0.004$  and  $J_S - K2 = 2.220 \pm 0.004$  mag for COCONUTS-3B using its SpeX prism spectrum, the dual-band K12 filters of SPHERE IRDIS, and a virtual  $J_S$  filter with 100% transmission spanning 1.2 –1.3  $\mu$ m adopted by Delorme et al. (2017). COCONUTS-3B is thus bluer than HD 206893B but still redder than field-age late-L dwarfs (see Figure 7 of Delorme et al. 2017).

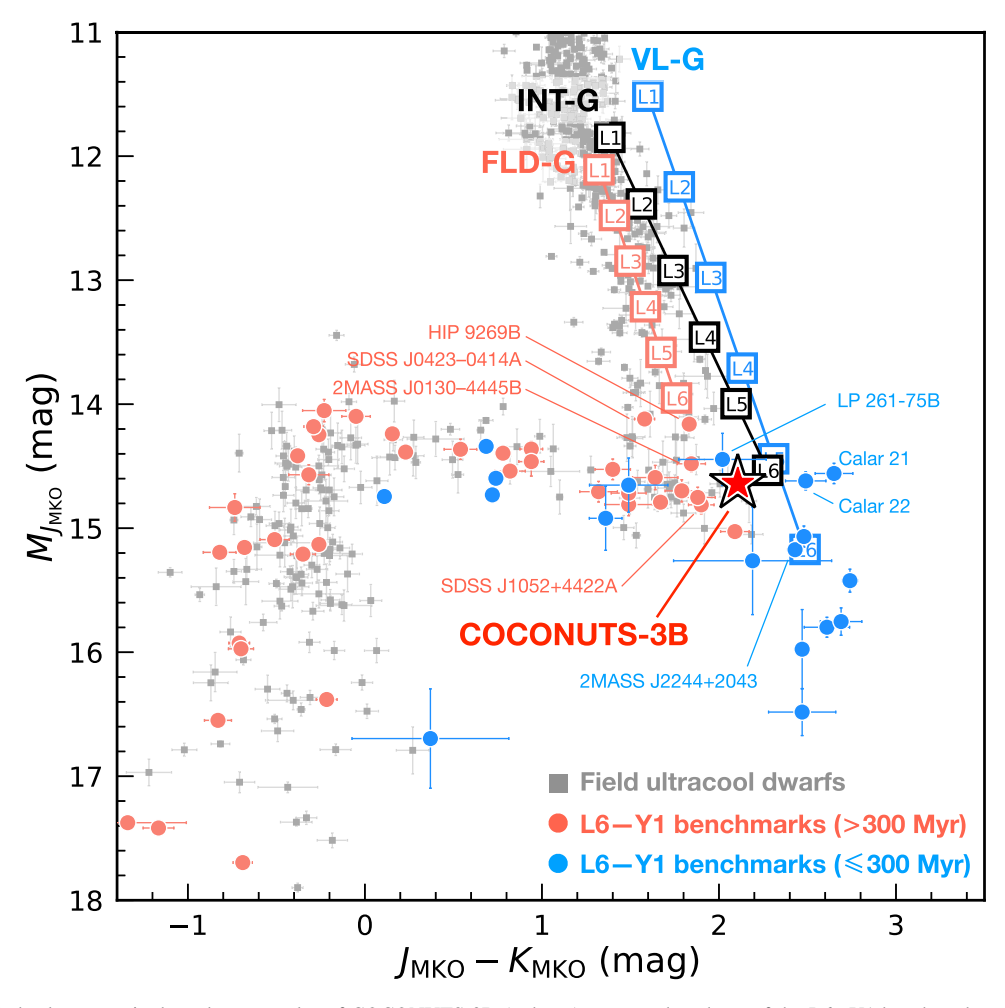


**Figure 12.** The *J*-band absolute magnitude and J - K color of COCONUTS-3B (red star) compared to those of the L6−Y1 benchmarks compiled by Zhang et al. (2020, 2021a) with ages of >300 (orange) and ≤300 (blue) Myr, as well as the photometric sequences of L1−L6 dwarfs with FLD-G (orange), INT-G (black), and VL-G (blue) gravity classes. We overlay the photometry of field dwarfs (gray) with M, L, T, and Y spectral types obtained from the UltracoolSheet (Best et al. 2020b), which have S/N > 5 in  $M_J$  and J - K and are not young, binaries, or subdwarfs. We label all benchmarks with the same spectral type (L6) as COCONUTS-3B, including HIP 9269B (Deacon et al. 2014), SDSSp J042348.57−041403.5A (SDSS J0423−0414A; Burgasser et al. 2005), 2MASS J01303563−4445411B (2MASS J0130−4445B; Reid et al. 2008; Dhital et al. 2011), SDSS J105213.51+442255.7A (SDSS J1052+4422A; Chiu et al. 2006; Dupuy et al. 2015), LP 261−75B (Kirkpatrick et al. 2000; Reid & Walkowicz 2006), 2MASS J2244+2043 (Dahn et al. 2002), and Calar 21 and Calar 22 (Zapatero Osorio et al. 2014). The J - K color of COCONUTS-3B is among the reddest compared to all benchmarks with ages of a few hundred megayears or older.

directly measured dynamical masses, meaning that the true mass of COCONUTS-3B might be as low as  $\sim 30 \, M_{\rm Jup}$ .

We construct the Saumon & Marley (2008) atmospheric model spectra at our derived evolution-based physical properties of COCONUTS-3B and compare them with the observed spectra. We find that models with  $f_{\rm SED}=1$  match the companion's spectrophotometry, although these models predict slightly brighter fluxes in the red optical, shallower depths for alkali resonance lines, a bluer *K*-band spectral slope, and fainter fluxes near 3.3  $\mu$ m. These data-model differences are very likely due to the older version of the opacity database used by Saumon & Marley (2008), and new sets of cloudy models that incorporate the theoretical advances of the past decade will likely improve the consistency between data and model predictions.

Compared to field-age, high-gravity L6 dwarfs, COCO-NUTS-3B has much fainter absolute magnitudes, similar bolometric luminosity, and a 120 K cooler effective temperature. This companion's J-K color is among the reddest of the ultracool benchmarks with ages older than a few hundred megayears. These anomalous spectrophotometric and physical

properties are in accord with its intermediate surface gravity, dusty atmosphere, and moderately young age, given the surface gravity dependence of the  $\rm L/T$  transition.

Similar to stellar binaries, the COCONUTS-3 system likely formed via fragmentation processes of the collapsing protostellar clouds, given the companion's mass and the large companion-to-host mass ratio (0.29  $\pm$  0.10). Under this formation scenario, COCONUTS-3B is expected to share the bulk metallicity and elemental abundances (e.g., C/O) of its host star. Modeling the spectroscopy of COCONUTS-3B and comparing the resulting chemical properties to those of COCONUTS-3A can directly quantify the systematic errors of the substellar and exoplanet model atmospheres. Expanding such calibration to a large ensemble of wide-orbit companions will enable thorough examination of model atmospheres over a wide parameter space, and these empirically calibrated models will lead to robust characterization of the atmospheric properties and formation of directly imaged exoplanets.

Z.Z. thanks Didier Saumon for sharing the Saumon & Marley (2008) atmospheric model spectra, Andre-Nicolas

Chene and Bin Yang for helpful discussions about the Gemini/ GMOS data reduction, Eric Mamajek for discussions about the typical photometric properties of dwarf stars, Andrew Mann for discussions about the empirical metallicity calibrations of young low-mass stars, Eunkyu Han for discussions about the magnetic fields in M dwarfs, and Adam Kraus and Brendan Bowler for helpful comments on the manuscript. Z.P.V. acknowledges the Heising-Simons Foundation for postdoctoral scholar support at Caltech. This work has benefited from The UltracoolSheet at http://bit.ly/UltracoolSheet, maintained by Will Best, Trent Dupuy, Michael Liu, Rob Siverd, and Zhoujian Zhang and developed from compilations by Dupuy & Liu (2012), Dupuy & Kraus (2013), Liu et al. (2016), Best et al. (2018), and Best et al. (2021). This research has benefited from the Ultracool RIZzo Spectral Library (https://doi.org/10. 5281/zenodo.11313), maintained by Jonathan Gagné and Kelle Cruz. This research has benefited from the Montreal Brown Dwarf and Exoplanet Spectral Library, maintained by Jonathan Gagné. This work is based in part on observations obtained at the international Gemini Observatory, a program of NSF's NOIRLab, which is managed by the Association of Universities for Research in Astronomy (AURA) under a cooperative agreement with the National Science Foundation on behalf of the Gemini Observatory partnership: the National Science Foundation (United States), National Research Council (Canada), Agencia Nacional de Investigación y Desarrollo (Chile), Ministerio de Ciencia, Tecnología e Innovación (Argentina), Ministério da Ciência, Tecnologia, Inovações e Comunicações (Brazil), and Korea Astronomy and Space Science Institute (Republic of Korea). This research has made use of the NASA/IPAC Infrared Science Archive, which is funded by the National Aeronautics and Space Administration and operated by the California Institute of Technology. This work has made use of data from the European Space Agency (ESA) mission Gaia (https://www.cosmos.esa.int/gaia), processed by the Gaia Data Processing and Analysis Consortium (DPAC; https://www.cosmos.esa.int/web/gaia/dpac/ consortium). Funding for the DPAC has been provided by

national institutions, in particular the institutions participating in the Gaia Multilateral Agreement.

\*Facilities: JJH 2.2m (SNIFS) Gemini (GMOS GNIRS)

Facilities: UH 2.2m (SNIFS), Gemini (GMOS, GNIRS), IRTF (SpeX).

Software: emcee (Foreman-Mackey et al. 2013), BANYAN  $\Sigma$  (version 1.2; Gagné et al. 2018), LACEWING (Riedel et al. 2017), TOPCAT (Taylor 2005), Astropy (Astropy Collaboration et al. 2013, 2018), IPython (Pérez & Granger 2007), Numpy (Oliphant 2006), Scipy (Jones et al. 2001), Matplotlib (Hunter 2007).

# Appendix A A Model-based Exploration of the Surface Gravity Dependence of the Empirical Metallicity Calibrations for Low-mass Stars

We estimated the bulk metallicity of COCONUTS-3A (Section 4.3) using empirical calibrations established by fieldage M dwarfs orbiting FGK primary stars, but these M-type calibrators have slightly higher surface gravities than the moderately young COCONUTS-3A. The metal-sensitive lines (e.g., Na I doublet at 2.2  $\mu m$ ) adopted by these calibrations are also sensitive to the surface gravity, meaning that our derived [Fe/H] $_{\star}$  may be unreliable. Here we use stellar model atmospheres to explore the surface gravity dependence of the

empirical calibrations of low-mass stellar metallicity as developed by Mann et al. (2013; M13), Mann et al. (2014; M14), and Newton et al. (2014; N14).

We base our analysis on the PHOENIX synthetic model spectra (Husser et al. 2013) over a parameter space of [2300, 4500] K in  $T_{\text{eff}}$ , [3.5, 5.5] dex in  $\log(g)$ , and [-1.0, +0.5] dex in [Fe/H] with intervals of 100 K, 0.5 dex, and 0.5 dex, respectively. We choose the range of  $T_{\rm eff}$  to cover the applicable spectral types (K5-M9.5) of all empirical calibrations considered here. The log(g) is also a proxy of stellar age, with log(g) = 5.5 dex corresponding to field ages (>1 Gyr), 5.0 dex for moderately young ages of 100 Myr to 1 Gyr, and 4.5 and 4.0 dex for very young ages of 5–100 Myr over the aforementioned parameter space (based on the evolution models of Baraffe et al. 2015). We downgrade the spectral resolution of these models to match that of SpeX SXD and put the model wavelengths in vacuum following Ciddor (1996). We then apply each calibration method to compute the empirical [Fe/H]<sub>emp</sub> for all model spectra that satisfy the method's applicable range in spectral type and metallicity. Specifically, we apply (1) the JHK-band calibration of Mann et al. (2013) to PHOENIX models with 4500 K  $\geqslant T_{\rm eff} \geqslant 3000$ K (i.e., K5–M5) and -1.04 dex  $\leq$  [Fe/H]  $\leq$  +0.56 dex, (2) the Mann et al. (2014) calibration to models  $3100 \,\mathrm{K} \geqslant T_{\mathrm{eff}} \geqslant 2300$ K M4.5-M9.5) (i.e., and  $-0.58 \, \text{dex} \leq [\text{Fe/H}] \leq +0.56 \, \text{dex}$ , and (3) the Newton et al. (2014) calibration to models with 3700 K  $\geqslant T_{\text{eff}} \geqslant 3000$  K (i.e., M1–M5) and  $-1.00 \, \text{dex} \leq [\text{Fe/H}] \leq +0.35 \, \text{dex}$ . The conversion between stellar effective temperatures and spectral types is based on the mean stellar properties compiled by E. Mamajek<sup>10</sup> (also see Pecaut & Mamajek 2013).

In Figures 13 and 14, we present the computed  $[Fe/H]_{emp}$  by various calibrations as a function of surface gravity. While one might expect that the  $[Fe/H]_{emp}$  at  $\log g = 5.5$  dex (i.e., field age of >1 Gyr) should all line up with the [Fe/H] of the models, our analysis shows that  $[Fe/H]_{emp}$  exhibit systematic,  $T_{eff}$  dependent offsets from the model [Fe/H] (e.g., see also Veyette et al. 2017). These mismatches are likely due to the systematic uncertainties of the stellar model atmospheres and the adopted opacity line lists (e.g., Figure 11 of Czekala et al. 2015) and that the calibrations considered here are all tied to the SpeX SXD instrument rather than the PHOENIX models. In other words, our analysis reaffirms the value of empirical metallicity calibrations as opposed to a purely model-based characterization.

Here we only focus on the trend (instead of the absolute values) of  $[Fe/H]_{emp}$  with respect to  $\log(g)$ . We first discuss the surface gravity effect on the Newton et al. (2014) and Mann et al. (2014) calibrations (Figure 13), which we use to derive the  $[Fe/H]_{\star}$  of COCONUTS-3A. For models with [Fe/H] = 0 and +0.5 dex, the Mann et al. (2014) calibration (applied to  $3100-2300 \, \mathrm{K}$ ) tends to derive a smaller  $[Fe/H]_{emp}$  toward lower surface gravities or younger ages. Specifically, compared to the case with  $\log(g) = 5.5 \, \mathrm{dex}$  (i.e., field age), the M14-based  $[Fe/H]_{emp}$  is smaller by 0.2–0.3 dex for the lower  $\log(g)$  of 5.0 dex and 0.5–0.6 dex for a  $\log(g)$  of 4.0 or 4.5 dex. The Newton et al. (2014) calibration (applied to 3700–3000 K) exhibits a similar trend with surface gravities for models with [Fe/H] = -1.0 (except for ones with  $T_{eff} = 3000 \, \mathrm{K}$ ), -0.5, and 0 dex. COCONUTS-3A has  $T_{eff} \approx 3000 \, \mathrm{K}$  and  $\log(g) \approx 5.0 \, \mathrm{M}$ 

 $<sup>\</sup>overline{^{10}}$  https://www.pas.rochester.edu/ẽmamajek/EEM\_dwarf\_UBVIJHK\_colors\_Teff.txt

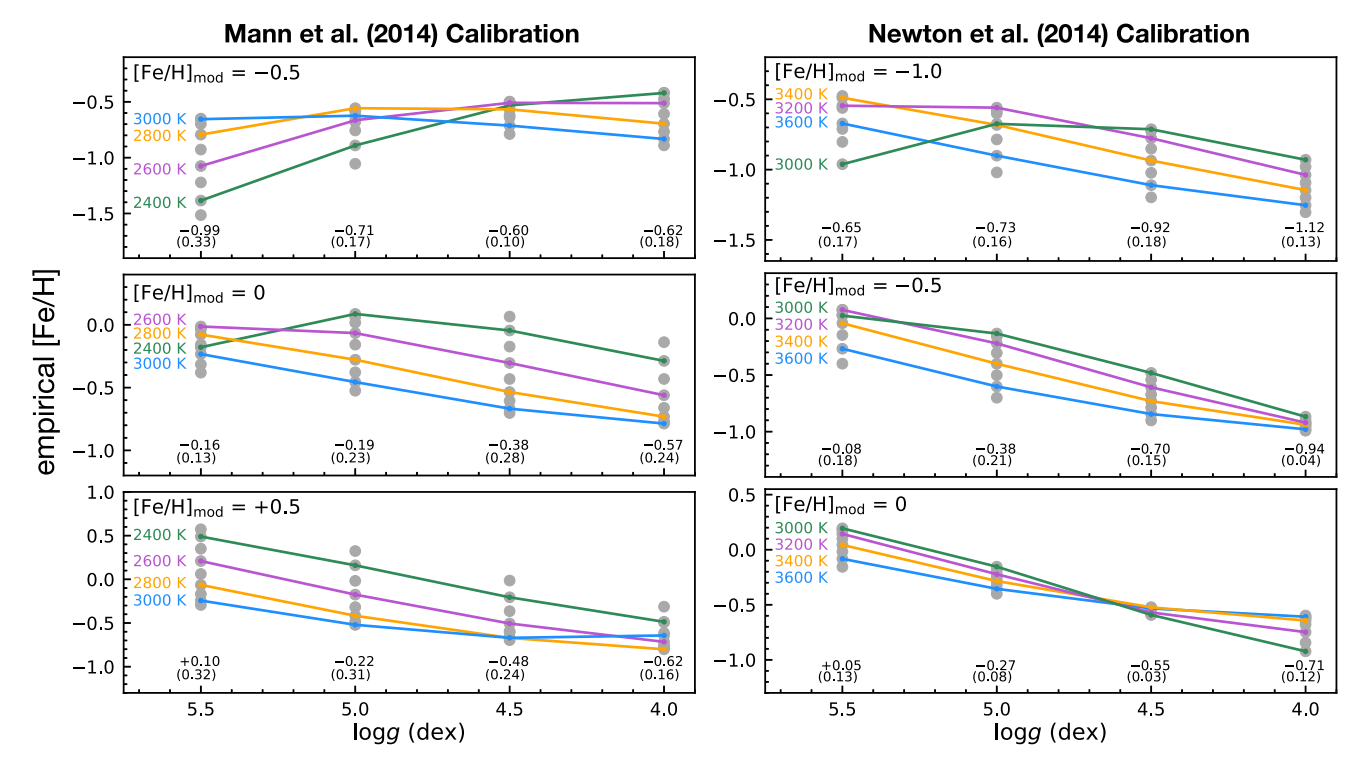


Figure 13. Computed empirical [Fe/H] (gray circles) of PHOENIX model spectra with different  $T_{\rm eff}$ ,  $\log(g)$ , and [Fe/H] using the calibrations of Mann et al. (2014; left panel) and Newton et al. (2014; right panel). The typical scatter of the Mann et al. (2014) and Newton et al. (2014) empirical calibrations is 0.07 and 0.12 dex, respectively. Surface gravity decreases from left to right in each panel, with  $\log(g) = 5.5$  dex corresponding to field ages (>1 Gyr), 5.0 dex for moderately young ages (100 Myr to 1 Gyr), and 4.5 and 4.0 dex for very young ages (5–100 Myr). Following the applicable range of each method, we apply the Mann et al. (2014) calibration to models with 3100 K  $\geqslant T_{\rm eff} \geqslant 2300$  K (M4.5–M9.5) and [Fe/H] = -0.5 (top left), 0 (middle left), and +0.5 (bottom left) dex and the Newton et al. (2014) calibration to models with 3700 K  $\geqslant T_{\rm eff} \geqslant 3000$  K (M1–M5) and [Fe/H] = -1 (top right), -0.5 (middle right), and 0 (bottom right) dex. We highlight a few equal- $T_{\rm eff}$  tracks in each panel, with a sequence of 3000 (blue), 2800 (orange), 2600 (purple), and 2400 (green) K for the Mann et al. (2014) calibration and 3600 (blue), 3400 (orange), 3200 (purple), and 3000 (green) K for the Newton et al. (2014) calibration. In each panel, we also label the mean and standard deviation (in parentheses) of the computed empirical [Fe/H] at each  $\log(g)$ .

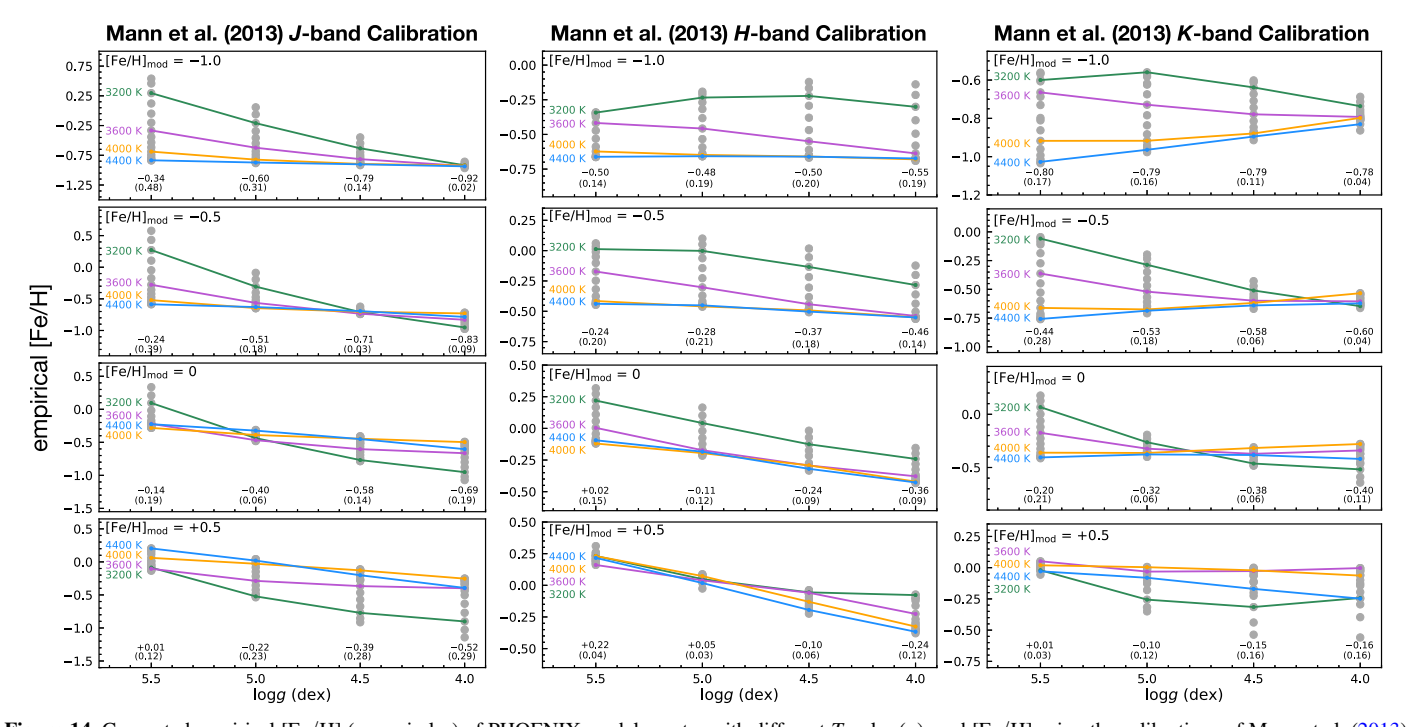


Figure 14. Computed empirical [Fe/H] (gray circles) of PHOENIX model spectra with different  $T_{\rm eff}$ ,  $\log(g)$ , and [Fe/H] using the calibrations of Mann et al. (2013) in the J (left panel), H (middle panel), and K (right panel) bands, with a similar format as Figure 13. The typical scatter of these JHK-band empirical calibrations is 0.12, 0.09, and 0.08 dex, respectively. Here we apply the Mann et al. (2013) calibration to models with 4500 K  $\geqslant T_{\rm eff} \geqslant 3000$  K (K5–M5) and [Fe/H] = -1 (first row), -0.5 (second row), 0 (third row), and +0.5 (fourth row) dex. The colored lines in each panel are equal- $T_{\rm eff}$  tracks corresponding to 4400 (blue), 4000 (orange), 3600 (purple), and 3200 (green) K.

 Table 5

 Properties of Background Stars Near COCONUTS-3A

Gaia EDR3 <sup>a</sup>					Gaia DR2					Estimated Properties				
Object	R.A. (hh:mm:ss.ss)	Decl. (dd:mm:ss.s)	Parallax (mas)	Distance (pc)	G (mag)	BP-RP (mag)	$M_G^{\ b}$ (mag)	Separation <sup>c</sup> (arcsec)	SpT	B-V (mag)	$\log(L_{ m bol}/L_{\odot}) \  m (dex)$	$\frac{\log(L_{\rm X}/L_{\rm bol})}{({\rm dex})}$	$F_{\rm X}$ (10 <sup>-15</sup> erg s <sup>-1</sup> cm <sup>-2</sup> )	
BG1	08:13:20.87	-15:25:40.2	$0.34 \pm 0.04$	$2596 \pm 276$	$16.045 \pm 0.001$	$0.775 \pm 0.004$	$3.97 \pm 0.23$	25.3	G0V	0.595	$0.13 \pm 0.05$	$-3.67 \pm 0.34$	≲1.37 ± 1.12	
BG2	08:13:14.56	-15:25:48.8	$0.46\pm0.02$	$2052 \pm 68$	$11.170 \pm 0.001$	$1.462 \pm 0.001$	$-0.39\pm0.07$	24.3	K giant				≲0.05	
BG3	08:13:14.66	-15:25:44.3	$0.08\pm0.14$	$11602 \pm 1867$	$18.261 \pm 0.002$	$0.445 \pm 0.022$	$2.94\pm0.35$	25.9	F1V	0.330	$0.79\pm0.08$	$-4.28\pm0.50$	$\lesssim$ 0.08 $\pm$ 0.09	
BG4	08:13:14.23	-15:25:38.9	$0.37\pm0.07$	$2773 \pm 420$	$17.037 \pm 0.001$	$0.852 \pm 0.008$	$4.82\pm0.33$	30.0	G5V	0.680	$-0.05\pm0.05$	$-3.71 \pm 0.47$	$\lesssim$ 0.72 $\pm$ 0.82	
BG5	08:13:16.45	-15:25:48.4	$0.27\pm0.50$	$2964 \pm 317$	$19.882 \pm 0.005$	$1.455 \pm 0.084$	$7.52\pm0.23$	14.2	K5V	1.150	$-0.76 \pm 0.10$	$-3.35 \pm 0.37$	$\lesssim$ 0.28 $\pm$ 0.26	
BG6	08:13:17.25	-15:25:47.2	$0.03\pm0.50$	$4872 \pm 612$	$19.771 \pm 0.005$	$1.214 \pm 0.105$	$6.33\pm0.27$	24.0	K3V	0.990	$-0.55 \pm 0.14$	$-3.35\pm0.37$	$\lesssim$ 0.17 $\pm$ 0.16	
BG7	08:13:17.30	-15:25:40.8	$0.39\pm0.07$	$2851 \pm 473$	$16.977 \pm 0.001$	$0.785 \pm 0.009$	$4.70\pm0.36$	28.7	G1V	0.622	$0.08\pm0.07$	$-3.67 \pm 0.34$	$\lesssim$ 1.01 $\pm$ 0.87	

#### Notes.

<sup>&</sup>lt;sup>a</sup> We provide Gaia EDR3 coordinates at epoch J2000 with equinox J2000 and the Bailer-Jones et al. (2021) distances.

b We compute G-band absolute magnitudes by combining the Gaia DR2 photometry and Gaia EDR3 distances.

<sup>&</sup>lt;sup>c</sup> Angular separations between the J2000 coordinates of background sources and the X-ray detection 2RXS J081318.4–152252.

dex (Section 4.4), so our derived  $[Fe/H]_{emp}$  might be underestimated by 0.2–0.3 dex according to these PHOENIX models. Qualitatively, this underestimate is expected, since a lower surface gravity can cause weaker strengths of the Na I doublet for early-to-mid-M stars (e.g., Luhman et al. 1998; Newton et al. 2014), and the [Fe/H] values by both Mann et al. (2014) and Newton et al. (2014) calibrations monotonically decrease with the decreasing EWs of Na I (as long as this EW is below 7.5 Å when applying the Newton et al. (2014) calibration).

Interestingly, surface gravity imposes the opposite effect on the Mann et al. (2014) calibration for models with [Fe/H] = -0.5 dex as compared to ones at higher metallicity (i.e., 0 and +0.5 dex), where the M14-based [Fe/H]<sub>emp</sub> tends to be larger with decreasing surface gravities. This means that the gravity dependence of the Na I doublet strengths at [Fe/H] = -0.5 dex and  $T_{\rm eff} < 3000$  K is different from the case with higher [Fe/H] and/or hotter  $T_{\rm eff}$ , according to the PHOENIX models.

The Mann et al. (2013) calibrations (Figure 14) also tend to derive smaller [Fe/H]<sub>emp</sub> toward lower surface gravities for models with cool  $T_{\rm eff}$  ( $\lesssim$ 3600 K) and solar or supersolar [Fe/H]. For hot, subsolar models with a  $T_{\rm eff}$  of  $\gtrsim$ 4000 K and [Fe/H] of -0.5 and -1 dex, the M13-based [Fe/H]<sub>emp</sub> can be comparable or even larger toward lower  $\log(g)$  compared to the case with  $\log(g) = 5.5$  dex.

Our analysis aims to provide a qualitative perspective on the surface gravity dependence of the empirical metallicity calibrations. We caution that the quantitative log(g) dependence revealed by our work should not be directly used as correction factors to the computed [Fe/H]<sub>emp</sub>, given that the systematics of the stellar model atmospheres likely change with surface gravities and effective temperatures as well. Also, compared to field-age low-mass stars, younger lower-gravity stars tend to be more active and possess stronger magnetic fields, which can alter the metal-sensitive line profiles and enhance the EWs (and thus the resulting [Fe/H]) via Zeimann broadening and intensification (e.g., Basri et al. 1992; Basri & Marcy 1994; Kochukhov 2021; López-Valdivia et al. 2021). Estimation of the bulk metallicity for low-gravity, low-mass stars would benefit from an empirical calibration customized for young stars, which is unfortunately not available to date. We note that this calibration is difficult to construct with the existing sample of nearby young stars, which lacks sufficiently large variations in [Fe/H] and mostly has solar metallicity.

## Appendix B Estimated X-Ray Emission from Background Stars Near COCONUTS-3A

Searching around COCONUTS-3A, we find a source, 2RXS J081318.4—152252 (2RXS J0813—1522), in the Second ROSAT All-Sky Survey and its counterpart, 1RXS J081318.4—152250 (1RXS J0813—1522), in the ROSAT All-Sky Survey Faint Source Catalog (Voges et al. 2000), with the latter catalog reporting a position error of 15". COCONUTS-3A is the closest match to both X-ray detections, with angular separations of 13".8 and 12".2, respectively. Seven background sources are also within 30" of 2RXS J0813—1522, but six are outside the 15" position error. Here we quantify the potential X-ray fluxes of all of these background stars to assess whether the ROSAT detection comes from COCONUTS-3A.

Figure 5 and Table 5 present the coordinates and photometry of the background sources (with distances of 2–12 kpc from Gaia EDR3), including six FGK dwarfs and one K-type giant star, based on their H-R diagram positions. For the dwarf stars, we convert BP-RP into spectral types and then obtain typical B-V and bolometric luminosities using the mean stellar colors and properties compiled by E. Mamajek (see footnote 10 and Pecaut & Mamajek 2013). We estimate the maximum possible X-ray fluxes of these objects by assuming that their X-ray emission is in the saturated regime. We obtain the saturated  $log(L_X/L_{bol})$  for each star based on Jackson et al. (2012) using the objects' B - V colors. We then compute the X-ray flux from each background dwarf star, with uncertainties in  $\log(L_{\rm bol}/L_{\odot})$ ,  $\log(L_{\rm X}/L_{\rm bol})$ , and distances propagated accordingly. The remaining giant star (BG2, TYC 5996–1259–1) falls in the asymptotic giant branch, evolving across the X-ray dividing line, and thereby has faint intrinsic X-ray emission. According to Maggio et al. (1990), the K giants have an X-rayto-V-band flux ratio of  $\log(F_{\rm X}/F_{\rm V})$  < -6.2, where  $\log(F_{\rm X}/F_{\rm V}) = \log(f_{\rm X}) + 0.4V + 5.47$ . We use this object's observed  $V = 11.57 \pm 0.14$  mag to compute its maximum possible X-ray flux.

Summing up our estimated X-ray fluxes of all background stars, we obtain  $(3.7\pm1.7)\times10^{-15}\,\mathrm{erg\,s^{-1}\,cm^{-2}}$ . This value is only  $2.2\%\pm1.6\%$  of the observed X-ray flux,  $(1.7\pm1.0)\times10^{-13}\,\mathrm{erg\,s^{-1}\,cm^{-2}}$ , of 2RXS J0813–1522 (Section 4.5.2), suggesting that the background sources in the neighborhood of COCONUTS-3A make a negligible contribution to our measured X-ray emission.

#### **ORCID iDs**

```
Zhoujian Zhang
(张周健) ® https://orcid.org/0000-0002-3726-4881
Michael C. Liu ® https://orcid.org/0000-0003-2232-7664
Caroline V. Morley ® https://orcid.org/0000-0002-4404-0456
Eugene A. Magnier ® https://orcid.org/0000-0002-7965-2815
Michael A. Tucker ® https://orcid.org/0000-0002-2471-8442
Zachary P. Vanderbosch ® https://orcid.org/0000-0002-0853-3464
Aaron Do ® https://orcid.org/0000-0003-3429-7845
Benjamin J. Shappee ® https://orcid.org/0000-0003-
```

#### References

```
Ackerman, A. S., & Marley, M. S. 2001, ApJ, 556, 872
Aldering, G., Adam, G., Antilogus, P., et al. 2002, Proc. SPIE, 4836, 61
Allard, N. F., Spiegelman, F., & Kielkopf, J. F. 2016, A&A, 589, A21
Allard, N. F., Spiegelman, F., Leininger, T., & Molliere, P. 2019, A&A,
  628, A120
Allers, K. N., & Liu, M. C. 2013, ApJ, 772, 79
Ansdell, M., Williams, J. P., van der Marel, N., et al. 2016, ApJ, 828, 46
Astropy Collaboration, Price-Whelan, A. M., Sipőcz, B. M., et al. 2018, AJ,
   156, 123
Astropy Collaboration, Robitaille, T. P., Tollerud, E. J., et al. 2013, A&A,
Bacon, R., Copin, Y., Monnet, G., et al. 2001, MNRAS, 326, 23
Bailer-Jones, C. A. L., Rybizki, J., Fouesneau, M., Demleitner, M., &
  Andrae, R. 2021, AJ, 161, 147
Baraffe, I., Homeier, D., Allard, F., & Chabrier, G. 2015, A&A, 577, A42
Barrado y Navascués, D., & Martín, E. L. 2003, AJ, 126, 2997
Barrado y Navascués, D., Stauffer, J. R., & Jayawardhana, R. 2004, ApJ,
Basri, G., & Marcy, G. W. 1994, ApJ, 431, 844
Basri, G., Marcy, G. W., & Valenti, J. A. 1992, ApJ, 390, 622
Bell, C. P. M., Mamajek, E. E., & Naylor, T. 2015, MNRAS, 454, 593
```

4631-1149

```
Bellm, E. C., Kulkarni, S. R., Graham, M. J., et al. 2019, PASP, 131, 018002
Best, W. M. J., Dupuy, T. J., Liu, M. C., Siverd, R. J., & Zhang, Z. 2020b, The
   UltracoolSheet: Photometry, Astrometry, Spectroscopy, and Multiplicity for
   3000+ Ultracool Dwarfs and Imaged Exoplanets, Zenodo, doi:10.5281/
   zenodo 4169085
Best, W. M. J., Liu, M. C., Magnier, E. A., & Dupuy, T. J. 2021, AJ, 161, 42
Best, W. M. J., Magnier, E. A., Liu, M. C., et al. 2018, ApJS, 234, 1
Binks, A. S., & Jeffries, R. D. 2014, MNRAS, 438, L11
Binks, A. S., & Jeffries, R. D. 2016, MNRAS, 455, 3345
Bohn, A. J., Ginski, C., Kenworthy, M. A., et al. 2021, A&A, 648, A73
Bohn, A. J., Kenworthy, M. A., Ginski, C., et al. 2020, ApJL, 898, L16
Boller, T., Freyberg, M. J., Trümper, J., et al. 2016, A&A, 588, A103
Bonfils, X., Delfosse, X., Udry, S., et al. 2005, A&A, 442, 635
Booth, R. S., Poppenhaeger, K., Watson, C. A., Silva Aguirre, V., & Wolk, S. J. 2017, MNRAS, 471, 1012
Boss, A. P. 2006, ApJL, 637, L137
Brandt, G. M., Dupuy, T. J., Li, Y., et al. 2021, AJ, 162, 301
Brandt, T. D., Dupuy, T. J., & Bowler, B. P. 2019, AJ, 158, 140
Brandt, T. D., & Huang, C. X. 2015, ApJ, 807, 58
Burgasser, A. J. 2007, ApJ, 659, 655
Burgasser, A. J. 2014, in Astronomical Society of India Conf. Ser. 11,
   Astronomical Society of India Conference Series, ed. H. P. Singh,
   P. Prugniel, & I. Vauglin (Hyderabad: ASI), 7
Burgasser, A. J., Cruz, K. L., Cushing, M., et al. 2010, ApJ, 710, 1142
Burgasser, A. J., Geballe, T. R., Leggett, S. K., Kirkpatrick, J. D., &
   Golimowski, D. A. 2006, ApJ, 637, 1067
Burgasser, A. J., Reid, I. N., Leggett, S. K., et al. 2005, ApJL, 634, L177
Chabrier, G. 2003, PASP, 115, 763
Chabrier, G., & Baraffe, I. 1997, A&A, 327, 1039
Chambers, K. C., Magnier, E. A., Metcalfe, N., et al. 2016, arXiv:1612.05560
Chiu, K., Fan, X., Leggett, S. K., et al. 2006, AJ, 131, 2722
Choi, J., Dotter, A., Conroy, C., et al. 2016, ApJ, 823, 102
Ciddor, P. E. 1996, ApOpt, 35, 1566
Cifuentes, C., Caballero, J. A., Cortés-Contreras, M., et al. 2020, A&A,
   642, A115
Cohen, M., Wheaton, W. A., & Megeath, S. T. 2003, AJ, 126, 1090
Covey, K. R., Ivezić, Ž., Schlegel, D., et al. 2007, AJ, 134, 2398
Cruz, K., & Gagné, J. 2014, The Ultracool RIZzo Spectral Library, Zenodo,
  doi:10.5281/zenodo.11313
Cruz, K. L., Burgasser, A. J., Reid, I. N., & Liebert, J. 2004, ApJL, 604, L61
Cruz, K. L., Kirkpatrick, J. D., & Burgasser, A. J. 2009, AJ, 137, 3345
Cruz, K. L., Núñez, A., Burgasser, A. J., et al. 2018, AJ, 155, 34
Cruz, K. L., Reid, I. N., Liebert, J., Kirkpatrick, J. D., & Lowrance, P. J. 2003,
    AJ, 126, 2421
Currie, T., Brandt, T. D., Kuzuhara, M., et al. 2020, ApJL, 904, L25
Cushing, M. C., Marley, M. S., Saumon, D., et al. 2008, ApJ, 678, 1372
Cushing, M. C., Rayner, J. T., & Vacca, W. D. 2005, ApJ, 623, 1115
Cushing, M. C., Vacca, W. D., & Rayner, J. T. 2004, PASP, 116, 362
Cutri, R. M., Skrutskie, M. F., van Dyk, S., et al. 2003, VizieR Online Data
   Catalog: 2MASS All-Sky Catalog of Point Sources
Cutri, R. M. e. 2014, VizieR On-line Data Catalog: II/328
Czekala, I., Andrews, S. M., Mandel, K. S., Hogg, D. W., & Green, G. M.
   2015, ApJ, 812, 128
Dahm, S. E. 2015, ApJ, 813, 108
Dahn, C. C., Harris, H. C., Vrba, F. J., et al. 2002, AJ, 124, 1170
Dawson, K. S., Schlegel, D. J., Ahn, C. P., et al. 2013, AJ, 145, 10
Deacon, N. R., Liu, M. C., Magnier, E. A., et al. 2014, ApJ, 792, 119
Delorme, P., Schmidt, T., Bonnefoy, M., et al. 2017, A&A, 608, A79
Dhital, S., Burgasser, A. J., Looper, D. L., & Stassun, K. G. 2011, AJ, 141, 7
Dhital, S., West, A. A., Stassun, K. G., et al. 2012, AJ, 143, 67
Dotter, A. 2016, ApJS, 222, 8
Douglas, S. T., Agüeros, M. A., Covey, K. R., et al. 2014, ApJ, 795, 161
Douglas, S. T., Curtis, J. L., Agüeros, M. A., et al. 2019, ApJ, 879, 100
Dupuy, T. J., & Kraus, A. L. 2013, Sci, 341, 1492
Dupuy, T. J., & Liu, M. C. 2012, ApJS, 201, 19
Dupuy, T. J., Liu, M. C., & Ireland, M. J. 2009, ApJ, 692, 729
Dupuy, T. J., Liu, M. C., & Ireland, M. J. 2014, ApJ, 790, 133
Dupuy, T. J., Liu, M. C., Leggett, S. K., et al. 2015, ApJ, 805, 56
Elias, J. H., Joyce, R. R., Liang, M., et al. 2006, Proc. SPIE, 6269, 62694C
Faherty, J. K., Riedel, A. R., Cruz, K. L., et al. 2016, ApJS, 225, 10
Filippazzo, J. C., Rice, E. L., Faherty, J., et al. 2015, ApJ, 810, 158
Findeisen, K., Hillenbrand, L., & Soderblom, D. 2011, AJ, 142, 23
Fleming, T. A., Molendi, S., Maccacaro, T., & Wolter, A. 1995, ApJS, 99, 701
Foreman-Mackey, D., Hogg, D. W., Lang, D., & Goodman, J. 2013, PASP,
   125, 306
Freedman, R. S., Marley, M. S., & Lodders, K. 2008, ApJS, 174, 504
```

```
Gaia Collaboration, Babusiaux, C., van Leeuwen, F., et al. 2018a, A&A,
  616, A10
Gaia Collaboration, Brown, A. G. A., Vallenari, A., et al. 2018b, A&A,
  616, A1
Gaia Collaboration, Brown, A. G. A., Vallenari, A., et al. 2021, A&A, 649, A1
Gagné, J., David, T. J., Mamajek, E. E., et al. 2020, ApJ, 903, 96
Artigau, É., Gagné, J., Faherty, J., et al. 2015, ApJ, 806, 254
Gagné, J., & Faherty, J. K. 2018, ApJ, 862, 138
Gagné, J., Lafrenière, D., Doyon, R., Malo, L., & Artigau, É. 2014, ApJ,
  783, 121
Gagné, J., Mamajek, E. E., Malo, L., et al. 2018, ApJ, 856, 23
Gizis, J. E., Allers, K. N., Liu, M. C., et al. 2015, ApJ, 799, 203
Gizis, J. E., Faherty, J. K., Liu, M. C., et al. 2012, AJ, 144, 94
Hewett, P. C., Warren, S. J., Leggett, S. K., & Hodgkin, S. T. 2006, MNRAS,
  367, 454
Hook, I. M., Jørgensen, I., Allington-Smith, J. R., et al. 2004, PASP, 116, 425
Hunter, J. D. 2007, CSE, 9, 90
Husser, T. O., Wende-von Berg, S., Dreizler, S., et al. 2013, A&A, 553, A6
Jackson, A. P., Davis, T. A., & Wheatley, P. J. 2012, MNRAS, 422, 2024
Johnson, J. A., Gazak, J. Z., Apps, K., et al. 2012, AJ, 143, 111
Jones, E., Oliphant, T., Peterson, P., et al. 2001, SciPy: Open source scientific
  tools for Python, http://www.scipy.org/
Kellogg, K., Metchev, S., Geißler, K., et al. 2015, AJ, 150, 182
Kenyon, S. J., & Hartmann, L. 1995, ApJS, 101, 117
Kesseli, A. Y., West, A. A., Veyette, M., et al. 2017, ApJS, 230, 16
Kiman, R., Faherty, J. K., Cruz, K. L., et al. 2021, AJ, 161, 277
Kirkpatrick, J. D., Cushing, M. C., Gelino, C. R., et al. 2011, ApJS, 197, 19
Kirkpatrick, J. D., Gelino, C. R., Faherty, J. K., et al. 2021, ApJS, 253, 7
Kirkpatrick, J. D., Looper, D. L., Burgasser, A. J., et al. 2010, ApJS, 190, 100
Kirkpatrick, J. D., Reid, I. N., Liebert, J., et al. 1999, ApJ, 519, 802
Kirkpatrick, J. D., Reid, I. N., Liebert, J., et al. 2000, AJ, 120, 447
Kochukhov, O. 2021, A&ARv, 29, 1
Kraus, A. L., Herczeg, G. J., Rizzuto, A. C., et al. 2017, ApJ, 838, 150
Kroupa, P. 2001, MNRAS, 322, 231
Kupfer, T., Prince, T. A., van Roestel, J., et al. 2021, MNRAS, 505, 1254
Lantz, B., Aldering, G., Antilogus, P., et al. 2004, Proc. SPIE, 5249, 146
Lépine, S., Rich, R. M., & Shara, M. M. 2007, ApJ, 669, 1235
Lindegren, L. 2018, Re-normalising the astrometric chi-square in Gaia DR2
  GAIA-C3-TN-LU-LL-124-01, ESA
Liu, M. C., Dupuy, T. J., & Allers, K. N. 2016, ApJ, 833, 96
Liu, M. C., Fischer, D. A., Graham, J. R., et al. 2002, ApJ, 571, 519
Liu, M. C., Magnier, E. A., Deacon, N. R., et al. 2013, ApJL, 777, L20
Looper, D. L., Kirkpatrick, J. D., Cutri, R. M., et al. 2008, ApJ, 686, 528
López-Valdivia, R., Sokal, K. R., Mace, G. N., et al. 2021, ApJ, 921, 53
Luhman, K. L., Briceño, C., Rieke, G. H., & Hartmann, L. 1998, ApJ, 493, 909
Lyo, A. R., Lawson, W. A., & Bessell, M. S. 2004, MNRAS, 355, 363
Macintosh, B., Graham, J. R., Barman, T., et al. 2015, Sci, 350, 64
Maggio, A., Vaiana, G. S., Haisch, B. M., et al. 1990, ApJ, 348, 253
Magnier, E. A., Schlafly, E. F., Finkbeiner, D. P., et al. 2020, ApJS, 251, 6
Maire, A. L., Baudino, J. L., Desidera, S., et al. 2020, A&A, 633, L2
Malo, L., Artigau, É., Doyon, R., et al. 2014, ApJ, 788, 81
Malo, L., Doyon, R., Lafrenière, D., et al. 2013, ApJ, 762, 88
Manara, C. F., Morbidelli, A., & Guillot, T. 2018, A&A, 618, L3
Mann, A. W., Brewer, J. M., Gaidos, E., Lépine, S., & Hilton, E. J. 2013, AJ,
Mann, A. W., Deacon, N. R., Gaidos, E., et al. 2014, AJ, 147, 160
Mann, A. W., Dupuy, T., Kraus, A. L., et al. 2019, ApJ, 871, 63
Mann, A. W., Feiden, G. A., Gaidos, E., Boyajian, T., & von Braun, K. 2015,
   ApJ, 804, 64
Marley, M. S., & Robinson, T. D. 2015, ARA&A, 53, 279
Marley, M. S., Saumon, D., Cushing, M., et al. 2012, ApJ, 754, 135
Marley, M. S., Saumon, D., Visscher, C., et al. 2021, ApJ, 920, 85
Marocco, F., Eisenhardt, P. R. M., Fowler, J. W., et al. 2021, ApJS, 253, 8
Marois, C., Macintosh, B., Barman, T., et al. 2008, Sci, 322, 1348
Marois, C., Zuckerman, B., Konopacky, Q. M., Macintosh, B., & Barman, T.
  2010, Natur, 468, 1080
Martin, D. C., Fanson, J., Schiminovich, D., et al. 2005, ApJL, 619, L1
Masci, F. J., Laher, R. R., Rusholme, B., et al. 2019, PASP, 131, 018003
McLean, I. S., McGovern, M. R., Burgasser, A. J., et al. 2003, ApJ, 596, 561
McMahon, R. G., Banerji, M., Gonzalez, E., et al. 2013, Msngr, 154, 35
Mentuch, E., Brandeker, A., van Kerkwijk, M. H., Jayawardhana, R., &
  Hauschildt, P. H. 2008, ApJ, 689, 1127
Metchev, S. A., & Hillenbrand, L. A. 2006, ApJ, 651, 1166
Milli, J., Hibon, P., Christiaens, V., et al. 2017, A&A, 597, L2
Murphy, S. J., & Lawson, W. A. 2015, MNRAS, 447, 1267
Neves, V., Bonfils, X., Santos, N. C., et al. 2012, A&A, 538, A25
```

```
Newton, E. R., Charbonneau, D., Irwin, J., et al. 2014, AJ, 147, 20
Newton, E. R., Irwin, J., Charbonneau, D., et al. 2017, ApJ, 834, 85
Oliphant, T. 2006, NumPy: A guide to NumPy (USA: Trelgol Publishing)
  http://www.numpy.org/
Pascucci, I., Testi, L., Herczeg, G. J., et al. 2016, ApJ, 831, 125
Paxton, B., Bildsten, L., Dotter, A., et al. 2011, ApJS, 192, 3
Pecaut, M. J., & Mamajek, E. E. 2013, ApJS, 208, 9
Pérez, F., & Granger, B. E. 2007, CSE, 9, 21
Preibisch, T., & Feigelson, E. D. 2005, ApJS, 160, 390
Gaia Collaboration, Prusti, T., de Bruijne, J. H. J., et al. 2016, A&A, 595, A1
Rayner, J. T., Cushing, M. C., & Vacca, W. D. 2009, ApJS, 185, 289
Rayner, J. T., Toomey, D. W., Onaka, P. M., et al. 2003, PASP, 115, 362
Rebull, L. M., Stauffer, J. R., Cody, A. M., et al. 2018, AJ, 155, 196
Reid, I. N., Cruz, K. L., Kirkpatrick, J. D., et al. 2008, AJ, 136, 1290
Reid, I. N., & Walkowicz, L. M. 2006, PASP, 118, 671
Riedel, A. R., Blunt, S. C., Lambrides, E. L., et al. 2017, AJ, 153, 95
Riedel, A. R., Finch, C. T., Henry, T. J., et al. 2014, AJ, 147, 85
Rodriguez, D. R., Zuckerman, B., Kastner, J. H., et al. 2013, ApJ, 774, 101
Rojas-Ayala, B., Covey, K. R., Muirhead, P. S., & Lloyd, J. P. 2010, ApJL,
   720, L113
Rojas-Ayala, B., Covey, K. R., Muirhead, P. S., & Lloyd, J. P. 2012, ApJ,
Ryabchikova, T., Piskunov, N., Kurucz, R. L., et al. 2015, PhyS, 90, 054005
Saumon, D., & Marley, M. S. 2008, ApJ, 689, 1327
Saumon, D., Marley, M. S., Abel, M., Frommhold, L., & Freedman, R. S.
   2012, ApJ, 750, 74
Schlaufman, K. C., & Laughlin, G. 2010, A&A, 519, A105
Schlieder, J. E., Lépine, S., Rice, E., et al. 2012a, AJ, 143, 114
Schlieder, J. E., Lépine, S., & Simon, M. 2012b, AJ, 143, 80
Schmidt, S. J., Hawley, S. L., West, A. A., et al. 2015, AJ, 149, 158
Schneider, A. C., Cushing, M. C., Kirkpatrick, J. D., et al. 2014, AJ, 147, 34
Schneider, A. C., & Shkolnik, E. L. 2018, AJ, 155, 122
Schneider, A. C., Windsor, J., Cushing, M. C., Kirkpatrick, J. D., &
   Shkolnik, E. L. 2017, AJ, 153, 196
Shappee, B. J., Prieto, J. L., Grupe, D., et al. 2014, ApJ, 788, 48
Shkolnik, E., Liu, M. C., & Reid, I. N. 2009, ApJ, 699, 649
Showman, A. P., Tan, X., & Parmentier, V. 2020, SSRv, 216, 139
```

```
Silaj, J., & Landstreet, J. D. 2014, A&A, 566, A132
Slesnick, C. L., Carpenter, J. M., & Hillenbrand, L. A. 2006a, AJ, 131, 3016
Slesnick, C. L., Carpenter, J. M., Hillenbrand, L. A., & Mamajek, E. E. 2006b,
  AJ, 132, 2665
Soderblom, D. R. 2010, ARA&A, 48, 581
Stassun, K. G., Oelkers, R. J., Paegert, M., et al. 2019, AJ, 158, 138
Taylor, M. B. 2005, in ASP Conf. Ser. 347, Astronomical Data Analysis
  Software and Systems XIV, ed. P. Shopbell, M. Britton, & R. Ebert (San
  Francisco, CA: ASP), 29
Terrien, R. C., Mahadevan, S., Bender, C. F., et al. 2012, ApJL, 747, L38
Tremblin, P., Amundsen, D. S., Chabrier, G., et al. 2016, ApJL, 817, L19
Tremblin, P., Chabrier, G., Baraffe, I., et al. 2017, ApJ, 850, 46
Vacca, W. D., Cushing, M. C., & Rayner, J. T. 2003, PASP, 115, 389
Veras, D., Crepp, J. R., & Ford, E. B. 2009, ApJ, 696, 1600
Veyette, M. J., Muirhead, P. S., Mann, A. W., et al. 2017, ApJ, 851, 26
Voges, W., Aschenbach, B., Boller, T., et al. 2000, IAU Circ., 7432, 3
Vrba, F. J., Henden, A. A., Luginbuhl, C. B., et al. 2004, AJ, 127, 2948
Walkowicz, L. M., Hawley, S. L., & West, A. A. 2004, PASP, 116, 1105
West, A. A., & Hawley, S. L. 2008, PASP, 120, 1161
West, A. A., Hawley, S. L., Bochanski, J. J., et al. 2008, AJ, 135, 785
West, A. A., Morgan, D. P., Bochanski, J. J., et al. 2011, AJ, 141, 97
Wright, E. L., Eisenhardt, P. R. M., Mainzer, A. K., et al. 2010, AJ, 140, 1868
Yurchenko, S. N., & Tennyson, J. 2014, MNRAS, 440, 1649
Yurchenko, S. N., Tennyson, J., Barber, R. J., & Thiel, W. 2013, JMoSp,
  291.69
Zapatero Osorio, M. R., Gálvez Ortiz, M. C., Bihain, G., et al. 2014, A&A,
  568, A77
Zhang, X. 2020, RAA, 20, 099
Zhang, Z., Liu, M. C., Best, W. M. J., et al. 2018, ApJ, 858, 41
Zhang, Z., Liu, M. C., Best, W. M. J., Dupuy, T. J., & Siverd, R. J. 2021a, ApJ,
Zhang, Z., Liu, M. C., Claytor, Z. R., et al. 2021b, ApJL, 916, L11
Zhang, Z., Liu, M. C., Hermes, J. J., et al. 2020, ApJ, 891, 171
Zhang, Z., Liu, M. C., Marley, M. S., Line, M. R., & Best, W. M. J. 2021c,
  ApJ, 916, 53
Zuckerman, B., & Song, I. 2004, ARA&A, 42, 685
```